



UNIVERSITY OF SOUTHAMPTON

**Inverse Design Tool for Multi-Element Wing  
Sections in Ground Effect**

Olle Nilsson

Completed under the supervision of

Dr. Davide Lasagna

Faculty of Engineering and Physical Sciences  
University of Southampton

Word Count:9896

This report is submitted in partial fulfilment of the requirements for the MEng Aeronautics & Astronautics, Faculty of Engineering and Physical Sciences, University of Southampton.



## **Abstract**

Regulatory restrictions on computational resource in Formula 1 opens up for the use of lower cost, lower fidelity, design tools to complement conventional CFD in the design process. Such a tool is the subject of this work.

This tool is developed using a potential-flow based panel method, aimed at the analysis and design of multi-element wing sections in ground effect with a target application towards Formula 1 front wing design. The tool has two methods: one for analysis considerations, where aerodynamics of wing sections are predicted based on potential-flow theory, and one for inverse design, where the pressure distribution can be prescribed over segments of the elements in a wing section, and the corresponding geometry solved for. A Python based tool implementing these methods has been developed and made available via GitHub, where a short user guide also can be found. Validation of the tool using theoretical results shows both methods to be accurate and have low computational cost.

Considering this, further extensions of the tool capability is suggested as future work, where a full-inverse design model could be implemented together with a viscous-inviscid interaction model for prediction of viscous boundary layer effects.

## Declaration

I, Olle Nilsson declare that this thesis and the work presented in it are my own and has been generated by me as the result of my own original research. I confirm that:

- 1) This work was done wholly or mainly while in candidature for a degree at this University;
- 2) Where any part of this thesis has previously been submitted for any other qualification at this University or any other institution, this has been clearly stated;
- 3) Where I have consulted the published work of others, this is always clearly attributed;
- 4) Where I have quoted from the work of others, the source is always given. With the exception of such quotations, this thesis is entirely my own work;
- 5) I have acknowledged all main sources of help;
- 6) Where the thesis is based on work done by myself jointly with others, I have made clear exactly what was done by others and what I have contributed myself;
- 7) None of this work has been published before submission.

## **Acknowledgements**

I would like to thank my supervisor, Dr. Davide Lasagna, for his guidance and support throughout this project.

A special thanks to Matthew Schofield at the Scuderia Toro Rosso Aerodynamics Department for providing a representative geometry to use in testing of the tool.

## Contents

<b>1</b>	<b>Introduction</b>	<b>1</b>
1.1	Organisation of Report . . . . .	3
<b>2</b>	<b>Background</b>	<b>4</b>
2.1	Multi-Element Wing Design: Considerations and Literature Review . . . . .	4
2.2	Literature Review of Potential-Flow Panel Methods . . . . .	5
2.2.1	Ground Effect . . . . .	6
2.2.2	Inverse Methods . . . . .	6
<b>3</b>	<b>Aim and Objectives</b>	<b>8</b>
<b>4</b>	<b>Methodology</b>	<b>9</b>
4.1	Potential-Flow Analysis Method . . . . .	9
4.2	Post Processing . . . . .	16
4.3	Potential-Flow Design Method . . . . .	20
<b>5</b>	<b>Validation</b>	<b>26</b>
5.1	Analysis Validation . . . . .	26
5.1.1	Single Element Analysis Validation . . . . .	26
5.1.2	Ground Effect Analysis Validation . . . . .	27
5.1.3	Multi-Element Analysis Validation . . . . .	28
5.2	Design Validation . . . . .	30
5.2.1	Single Element Design Validation . . . . .	30
5.2.2	Ground Effect Design Validation . . . . .	31
5.2.3	Multi-Element Design Validation . . . . .	33
<b>6</b>	<b>Example Design Cases</b>	<b>36</b>
6.1	Smoothing Surface Pressure Peaks . . . . .	36
6.2	Ground Clearance Envelope Optimisation . . . . .	37
6.3	Demonstration of Pressure Distribution Degrees of Freedom (A and B constants)	40
6.4	Representative Analysis and Design Case: Scuderia Toro Rosso STR10 Y-400 Front Wing Section . . . . .	43

---

6.5 Post-Processing Examples . . . . .	45
<b>7 Discussion on Limitations</b>	<b>46</b>
<b>8 Summary, Conclusions and Outlook</b>	<b>48</b>
<b>References</b>	<b>49</b>

## Nomenclature

$a_{ij}$	=	streamfunction influence coefficient
$A$	=	weighting constant of $g$
$B$	=	weighting constant of $h$
$c$	=	chord length
$C_L$	=	lift coefficient
$C_P$	=	pressure coefficient
$C_z$	=	downforce(negative z-force) coefficient
$\mathbf{D}$	=	diagonal scaling matrix
$\mathbf{F}$	=	objective function
$\mathbf{GC}$	=	vector from prospective solution for point $(x, z)$ normal to $\hat{n}$
$g$	=	$\gamma_i$ shape function #1
$h$	=	$\gamma_i$ shape function #2
$h/c$	=	wing section ground clearance as a fraction of total chord length
$\mathbf{J}$	=	Jacobian matrix
$K$	=	number of elements in section
$M$	=	number of panels per element
$N$	=	total number of bodies in solution = $K + K$
$N_x$	=	number of grid points on $x$ -direction
$N_z$	=	number of grid points on $z$ -direction
$\hat{n}$	=	surface normal direction unit vector
$n_1$	=	adjacent panel normal direction
$p$	=	general variable
$P$	=	general field point
$q_n$	=	surface normal velocity
$q_t$	=	surface tangential velocity
$r$	=	distance from point on $s$ to $P$
$s$	=	element surface coordinate
$S$	=	coordinate along A
$\delta s$	=	local panel-length
$u$	=	velocity in $x$ -direction
$u_{ij}$	=	$x$ -velocity influence coefficient
${}^1\hat{U}_j$	=	$x$ -velocity influence per unit strength of $\gamma_{j+1} + \gamma_j$
${}^2\hat{U}_j$	=	$x$ -velocity influence per unit strength of $\gamma_{j+1} - \gamma_j$
$U_\infty$	=	freestream velocity
$w$	=	velocity in $z$ -direction
$w_{ij}$	=	$z$ -velocity influence coefficient
${}^1\hat{W}_j$	=	$z$ -velocity influence per unit strength of $\gamma_{j+1} + \gamma_j$
${}^2\hat{W}_j$	=	$z$ -velocity influence per unit strength of $\gamma_{j+1} - \gamma_j$
$\mathbf{W}$	=	solution vector
$x, z$	=	global coordinates
$x^*, z^*$	=	local panel coordinates
$\alpha$	=	incidence angle of freestream flow



$\beta$	=	panel orientation angle
$\Gamma$	=	circulation
$\gamma$	=	circulation per unit length
$\theta$	=	angle of $r$
$\Psi$	=	streamfunction
${}^1\hat{\Psi}_j$	=	streamfunction influence per unit strength of $\gamma_{j+1} + \gamma_j$
${}^2\hat{\Psi}_j$	=	streamfunction influence per unit strength of $\gamma_{j+1} - \gamma_j$
$\Phi$	=	velocity potential

#### Subscripts

$( )_i$	=	boundary point index
$( )_{i_S}$	=	boundary point index at start of design segment
$( )_{i_E}$	=	boundary point index at end of design segment
$( )_j$	=	boundary point or panel index
$( )_k$	=	body index
$( )_{k_i}$	=	body index of boundary point $i$
$( )_{k_j}$	=	body index of boundary point $j$
$( )_\infty$	=	freestream condition

#### Superscripts

$( )^+$	=	prospective solution
---------	---	----------------------

#### Abbreviations

FIA	=	Federation Internationale de l'Automobile
LE	=	Leading Edge
RHS	=	right-hand side
TE	=	Trailing Edge

## 1 Introduction

The 1968 Monaco Grand Prix saw the introduction of wings into Formula 1 (F1). Team Lotus introduced an inverted wing mounted at the front of its Model 49, shown in a later configuration in Fig. 1. They would go on to win the race, and at the next round in Belgium several other teams followed this new concept, with Ferrari being the first to use a low mounted wing at the front, together with a high mounted wing at the rear. The “modern aerodynamic configuration” of Formula 1 cars was born.



**Fig. 1 Late 1968 Lotus 49. A high mounted rear wing had been introduced in addition to the front wing first used at the Monaco Grand Prix. Retrieved from <http://www.formula1-dictionary.net/wings.html>.**

While the effectiveness of these early designs can be questioned, their intention was clear: increased contact pressure between the tyre and the road-surface would increase lateral and longitudinal acceleration capabilities of the car. Brake later, negotiate the turn at higher speed, and accelerate away at a faster rate, leading to lower lap times. This same fundamental principle remains today, although Formula 1 has during the time grown to become a multi-billion-pound industry, where sophisticated computational fluid dynamics (CFD) tools and wind-tunnel facilities are used to aid the aerodynamic design process.

Today aerodynamic design in F1 is limited by a strict set of rules defined by motorsports governing body, Federation Internationale de l'Automobile (FIA), in their technical regulations [1]. An example of modern Formula 1 aerodynamic design is shown in Fig. 2. Also regulated through the FIA is the use of development tools, such as CFD and wind-tunnel facilities [2], with no on-track testing being allowed outside of FIA controlled sessions, usually amounting to only 8 days per year. These limits are put in place to ensure more parity between teams backed by car manufacturers, and privateers, who usually cannot match manufacturer backed budgets. Ultimately, this leads to the design process being limited by the allowed allocation of computational resource and wind-tunnel time. This limitation opens up for the use of lower cost, lower fidelity, design tools to complement conventional CFD in the design process. Such a tool is the subject of this work.



**Fig. 2** Example of a modern Formula 1 car. 2018 Scuderia Toro Rosso STR13. Retrieved from [https://www.motorsportimages.com/photos/?p=2&race\\_type\\_id=54](https://www.motorsportimages.com/photos/?p=2&race_type_id=54).

Modern CFD methods can be considered high fidelity, high cost, meaning that the results will be relatively accurate, but at a large computational expense compared to older methods. Generally, as the available computational power is increased, designers move to increasingly accurate, and costly, CFD methods [3]. Half a century ago, the so called panel-method was the state of the art of CFD. First developed in the early to mid 1950's at the Douglas Aircraft Company [4], it is based on approximating shapes by a series of linear segments. This approximation reduces the computation needed to evaluating algebraic relations and summing them, making it suitable for the computational power available at that time. The method was immediately successful in predicting the aerodynamics of aircraft fuselages [5] and wing sections [6]. It was also frequently used to calculate the shape corresponding to certain designer specified aerodynamics, so called inverse design, to great effect [7].

The panel-method remained popular into the 1990's, which saw the release of publicly available implementations, aimed at wing section analysis and design [8, 9]. On a standard modern PC, these programmes completes aerodynamic calculations of simple wing sections effectively instantly, making a panel-method suitable for the implementation of the proposed tool.

The aim of this work is thus to develop a tool based on a potential-flow panel-method, for analysing the typical wing sections seen in modern Formula 1. This tool shall then be extended to allow the pressure distribution to be prescribed over parts of each element in a section, and the corresponding geometry solved for. The tool is proposed to aid the conventional CFD process, where the available computational resource is limited, by providing the designer with an additional design option that is effectively cost-less, and provides results quickly, allowing the designer to use it interactively. The design process workflow with the proposed tool incorporated is shown in Fig. 3a, here the proposed tool is used for solving certain design problems that would normally require large amount of iteration using convectional CFD tools. This will save both computational and labour resource. The expanded tool-set available to the designer is shown in terms of accuracy vs. resource cost in Fig. 3b.

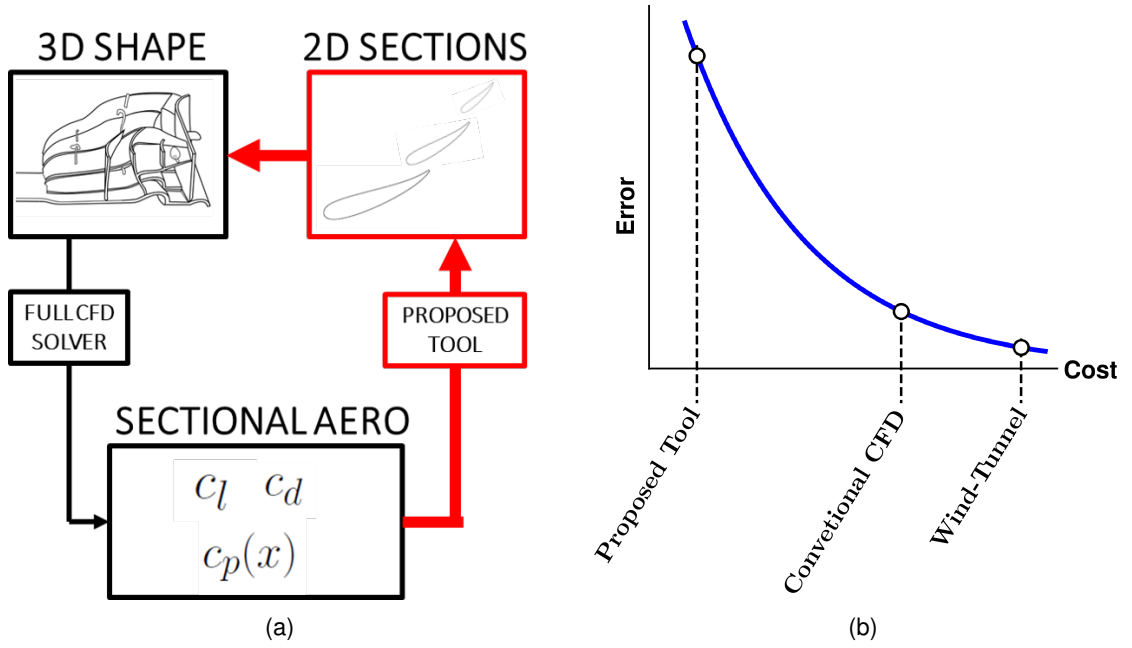


**Fig. 3 (a) Workflow of the complete design process with the proposed tool incorporated. (b) Designers available toolset with the proposed tool incorporated. Accuracy vs. resource cost visualised. Top left picture adapted from <https://www.f1technical.net/forum/viewtopic.php?t=21584>.**

## 1.1 Organisation of Report

The next section of this report presents a more detailed background to the project, beginning with some discussion about the ideas and challenges behind Formula 1 Wing Design, and then progresses to review the details of current potential-flow panel methods. In section 3 the detailed aim and objectives of this work is presented. The theoretical models for potential-flow analysis and design are developed in section 4, and their implementations validated in section 5. Some examples of design cases are shown in section 6. This includes a modern Formula 1 front wing section, which has been provided by the Scuderia Toro Rosso (STR) aerodynamics department, and was used during the 2015 season on their STR10. The limitations of the implementation is discussed in section 7. Section 8 rounds off the work with a summary of results, conclusions and some future outlook for continued development of this tool.

## 2 Background

In this section a discussion about the ideas and challenges behind Formula 1 Multi-Element Wing Design is first presented. This evolves around the flow physics phenomena of multi-element wings in ground effect found by previous work.

This is followed by a detailed literature review of potential-flow panel methods aimed at finding an appropriate approach for the theoretical formulation of the proposed tool.

### 2.1 Multi-Element Wing Design: Considerations and Literature Review

In Formula 1 wing design multi-element sections are exclusively used due to their capability of generating high loads. The physical arguments behind this originates from [10], and is summarised as follows:

**New Boundary-Layer Effect:** A wing section consisting of several shorter surfaces decreases the distance the flow needs to travel from the stagnation point until leaving the element at the trailing-edge (TE), meaning the boundary layer on each element needs to withstand any adverse pressure gradient for a shorter distance, compared to using fewer elements. This enables the designer to use steeper gradients when recovering pressure, effectively increasing suction toward the TE.

**Reduced Pressure Recovery Demand:** Having an element trailing another creates a low pressure field in the region where the flow leaves the leading elements TE. Effectively, the velocities in the direction tangential to the leading elements TE are larger than the freestream velocity, reducing the amount of pressure that needs to be recovered along the surface of the element.

**Off-Surface Pressure Recovery:** The pressure of the flow leaving the TE of an element can continue to recover in the adverse gradient pressure field of the elements behind it. This process is more effective than on-surface pressure recovery.

**Circulation Effects:** There are two beneficial circulation based effects of having an elements mounted consecutively:

- 1) A leading element has a circulation that opposes the flow-direction near the high curvature region of a trailing elements leading-edge (LE). This effect can be used to reduce suction-peaks at the trailing elements LE, where very large pressure gradients, leading to separation, could otherwise develop as ground clearance is reduced. In a well-designed multi-element wing section, such as the STR example shown in section 6.4, this effect is used to create immunity against pressure peaks at the LE of all trailing elements the a section. A possible design problem for the proposed tool could be tune this interaction between elements, to make full use of this effect.
- 2) The effect of circulation of a trailing element, which effectively increases the flow angle around the TE region of a leading element. The circulation of the leading element then needs to increase to match this flow angle at the TE.

Formula 1 front wings are operated in close proximity to the ground and its aerodynamic characteristics therefore heavily influenced by ground effect. This has been studied in [11–

13], where the restriction of the flow between the ground and the wings suction surface was found to significantly alter the pressure distribution, with peak  $C_p$  values increasing up to four times the free-air values at realistic ground clearances. Ground effect must thus be modelled, even for this low fidelity tool, to obtain meaningful results.

An inverted wing operates with the suction surface facing the ground, as opposed to an aircraft in ground effect. In [14], this was found to create a more critical condition, as the distance to the ground will have a large influence on pressure gradients, especially on the first element in a section, which can lead to flow separation. This shows the importance in being able to finely tune pressure gradients, especially on the first element in a section, to optimise loading behaviour between different ground clearances. This is one design problem targeted by the proposed tool, and will later be demonstrated in section 6.2.

Studies on inverted wings in ground effect have mostly been conducted using isolated wings, the effect of a front wing on the aerodynamic performance of other components of a race car are thus not considered. In [15] however, the adverse effects on overall aerodynamic load of a generic open-wheel race car operating in the velocity deficient wake of another car was shown. These adverse effects can be considered analogous to velocity deficits originating from the cars own front wing, that the rest of the car then has to operate in. In the design process the front wing thus needs to be considered only partially a force generating device, which is also used to setup the downstream flow conditions.

## 2.2 Literature Review of Potential-Flow Panel Methods

Based on the discussion in section 2.1, the tool needs to have the capability to:

- 1) Calculate the potential-flow around multi-element wing sections;
- 2) Account for ground effect in this calculation;
- 3) Be able to solve for the geometry corresponding to a user specified pressure distribution.

Although the effects of viscosity will not be considered at this time, having a formulation that could be extended to account for this will be prioritised as a future outlook.

When developing a potential-flow panel code there are three initial decisions that have to be made based on the intended application [16];

- 1) Selection of singularity element. Here the choice stands between source, doublet or vortex.
- 2) Choice of order for the singularity distribution.
- 3) Selection of boundary condition (BC). The options are: the Neumann BC, which specifies no flow normal to the boundary of the body. This BC is thus associated with a velocity based formulation. The Dirichlet BC, specifies a constant value along a boundary. This BC is thus associated with a velocity potential, or streamfunction based formulation.

A model with circulation is needed for predicting aerodynamic forces, which makes a source model unsuitable. From the results presented in [16–19], a linearly varying vortex distribution is much less sensitive to cusped(thin) TE geometries, with all other methods becoming

singular as the TE thickness approaches zero. Very thin trailing edges are common in the highly cambered elements usually used in multi-element application. Additionally [16, 18] both state that a linearly varying singularity strength is preferred when geometric boundaries are close to each other, as often the case in the overlapping region of multi-element wing sections.

### 2.2.1 Ground Effect

Modelling of ground effect in panel methods has been done for conventionally oriented wings aimed at aircraft applications. In [20, 21] the method of images is used, whereby the geometry subject to analysis is mirrored about the desired ground plane, and the flow solved accounting for the influence of the mirrored body. This creates a line of symmetry at the mirror plane, and thereby there can be no flow normal to this plane, simulating a solid boundary. Another method for modelling ground effect is used in [22], where a solid wall is added at desired ground plane as an additional body in the solution. Both methods are illustrated in Fig. 4.

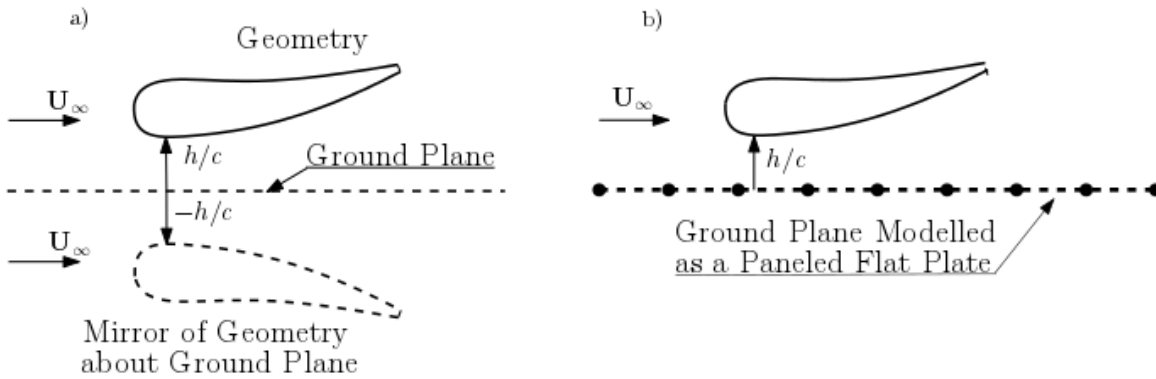


**Fig. 4 Two ways of modelling ground effect in panel methods: (a) Using a mirror image. (b) Having a panelled flat plate act as the ground plane.**

The second method has the advantage of resulting in less computational work as soon as the total amount of panels used to represent the wing section subject to analysis exceed the amount of panels needed for the representation of the solid wall, which is likely as soon as multiple elements are considered. For the method of images the amount of unknowns are always doubled, which increases the computation cost by a factor of 4 [23].

In using the method of images the formulation for considering ground effect will be identical to that of considering multiple elements, since it is simply a case of adding additional elements to the solution. This avoids having to develop a unique formulation for consider bodies that are not closed, and combining this with a normal formulation for closed bodies, as would be needed with the second method.

### 2.2.2 Inverse Methods

Many reviews on inverse methods using panel methods have been conducted. Recent examples that focuses on techniques relating wing-section are [24], where the more practical aspects of the methods are considered, and [25], which is more focused on the mathematical detail. Based on these works, inverse design methods can be grouped into two main

categories:

- 1) De-coupled methods where the geometry and aerodynamics are solved separately, and the process is iterated towards the specified solution. This consists of solving for the pressure distribution of a section, as in a regular panel solver, and using the error of the current sections pressure distribution to the specified values to make geometric alterations. The new shape is then fed back into the solver, and the process repeated the solution converges. A typical example using this type of solution is [26]. The main advantages of this method is the simplicity of the implementation, as the different parts of the program are not coupled together.
- 2) Coupled methods where the complete system of geometric and aerodynamic unknowns are solved simultaneously. This method is thus not iterative in the same sense as de-coupled methods, but the solution still requires iteration since the system is non-linear. A typical example using this approach is Xfoil [8]. Coupled solutions are more rare, likely due to its more complex implementation, but are quoted to be faster and more robust.

De-coupled methods are usually used with a velocity based approach and thus a Neumann BC which is inherently a more complex formulation, and usually slower than the approaches using the Dirichlet BC [16, 27].

According to [8], the streamfunction approach is ideal when considering viscous displacement effects. When considering viscosity the overall system becomes non-linear even for the analysis of wing-sections. This solution method is therefore very similar to the coupled inverse method. A coupled streamfunction based method would therefore be the simplest to extend to account for viscosity at a later time.

Considering the above, the tool in this work will be developed using a vortex singularity element of linearly varying strength, with a Dirichlet BC and a streamfunction based formulation. This is the same basic formulation used in Xfoil [8]. This formulation, as implemented in Xfoil, cannot handle multiple-elements, or ground effect, but will be extended to allow for this.



### 3 Aim and Objectives

Considering the regulatory limitations on computational resource for CFD development in Formula 1, a lower cost, lower fidelity, design tool to complement conventional CFD in the design process of multi-element wings is needed.

**Aim:** To develop a potential-flow based panel method tool for use in the analysis and design of multi-element wing sections in ground effect.

**Objectives:**

- 1) Develop a theoretical method for calculating the potential-flow around multi-element wing sections in ground effect. This is to be implemented as a Python computer program forming the analysis method of the tool;
- 2) Develop a theoretical method for extending the analysis method to allow the desired pressure distributions of the elements in a section to be prescribed, and the corresponding geometry solved for. This is to be implemented as a Python computer program forming the design method of the tool;
- 3) Validate the potential-flow analysis method against exact solutions;
- 4) Validate the potential-flow design method against known solutions;
- 5) Demonstrate the capabilities of the tool through some typical test cases.

## 4 Methodology

In this section a general method for analysing the aerodynamics of multi-element wing sections is first developed. This method is then extended to a design method where the desired pressure distributions of the elements in a section can be prescribed and the corresponding geometry solved for.

### 4.1 Potetial-Flow Analysis Method

The problem is modelled by considering a wing-section of  $K$ -elements and its mirror-image about the plane  $z = 0$ , resulting in a total of  $N$ -bodies in the field where  $N = K + K$ , as shown in Fig. 5. The mirror-image is used to model ground effect on the section by creating a flow-field symmetrical about the mirror plane. This ensures  $z = 0$  becomes a streamline in the flow, where by symmetry  $\Psi = 0$ , which can then be taken as the ground plane. Varying ground clearance can be considered by adjusting the distance of the section to the ground plane.

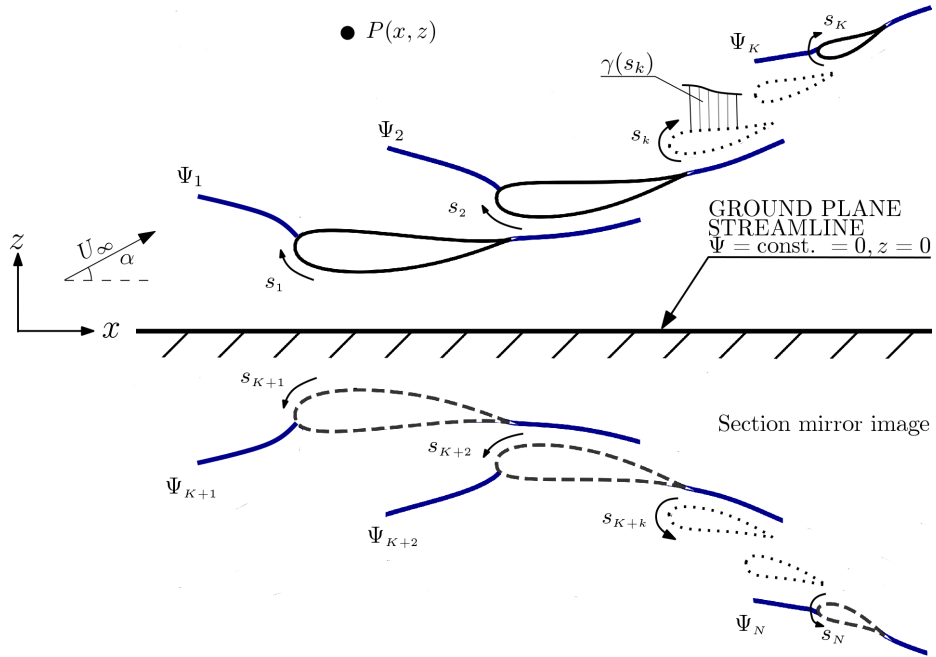


**Fig. 5 General model of the analysis method. A wing section of  $K$ -elements and its mirror-image is modelled as vortex sheets superpositioned with a freestream flow.**

A vortex sheet of strength per unit-length  $\gamma(s_k)$  is placed on the surface of each body, where  $s_k$  is a coordinate along the surface of the  $k$ -th element, defined to run clockwise for bodies in the section and counter-clockwise for bodies in the mirror image. A solution is sought for  $\gamma(s_k)$  ;  $1 \leq k \leq N$ , such that the superposition of the  $N$ -vortex sheets and a freestream flow creates a flow-field where the streamfunction takes a constant value on the surface of each body,  $\Psi = \Psi_k = \text{const.}$  ;  $1 \leq k \leq N$ .

The streamfunction contribution of a vortex sheet at a field point  $P(x, z)$  is obtained by analogy to the contribution of a point vortex with strength  $\Gamma$ , placed at  $(x_0, z_0)$ , as shown in Fig. 6a

$$\Psi_{vortex}(x, z) = \frac{\Gamma}{2\pi} \ln r(x, z, x_0, z_0), \quad (1)$$

where  $r$  is the distance from the point vortex center to the field point

$$r = \sqrt{(x - x_0)^2 + (z - z_0)^2}. \quad (2)$$

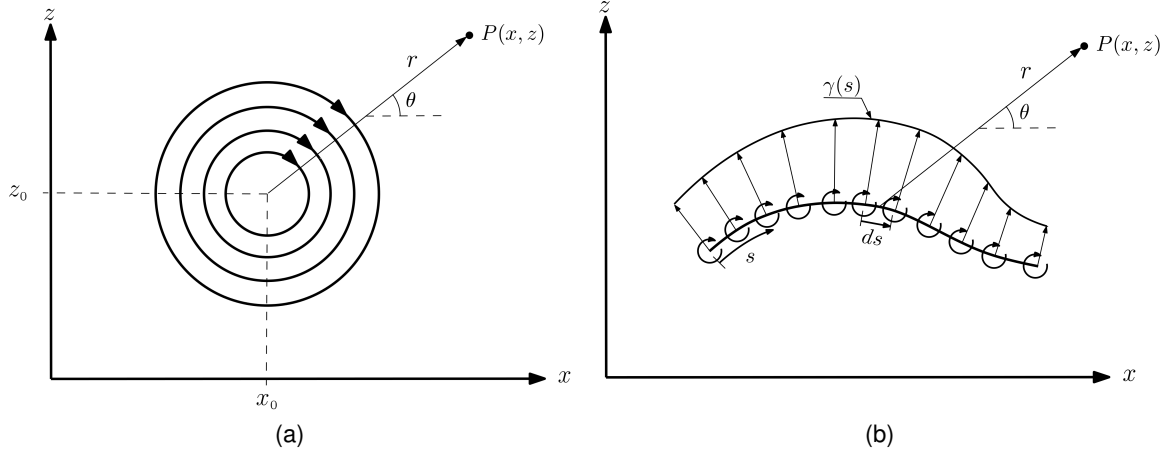


**Fig. 6 Nomenclature for calculating the streamfunction influence at a point  $P(x, z)$  for: (a) a point vortex of strength  $\Gamma$  located at  $(x_0, z_0)$ . (b) a vortex sheet of strength per unit length  $\gamma(s)$  placed along the path  $s$ .**

Similarly, for the vortex sheet in Fig. 6b of strength per unit length  $\gamma(s)$ , placed along the path  $s$ , the segment  $ds$  of the sheet can be taken as a point vortex providing  $ds$  is sufficiently small. The streamfunction contribution of this segment of  $s$  is then  $\frac{\gamma(s)ds}{2\pi} \ln r$ , and the total contribution of the sheet is this expression integrated along  $s$ .

The streamfunction value at a general point  $P(x, z)$  for the superposition of the  $N$ -vortex sheets and a freestream flow is then

$$\Psi(x, z) = U_\infty(z \cos \alpha - x \sin \alpha) + \frac{1}{2\pi} \sum_{k=1}^N \int \gamma(s_k) \ln r(s_k, x, z) ds_k, \quad (3)$$

where  $r$  is the distance from a point on  $s_k$ ,  $U_\infty$  the freestream velocity, and  $\alpha$  the incidence angle of the oncoming flow. Normally  $\alpha = 0$ , and the streamfunction contribution of the freestream reduces to  $U_\infty z$ , since the oncoming flow needs to be parallel to the ground plane.  $\alpha$  is still kept as a variable to allow simple variation of the incidence angle when considering cases out of ground effect. For cases in ground effect the incidence needs to be adjusted by a coordinate transformation of the geometry.

The streamfunction is chosen over velocity potential and velocity based methods to simplify the design method formulation, and to prepare for a future extension of the methods to handle viscous flows, where this approach is preferred to model boundary layer displacement effects [8]. The detailed advantages of the streamfunction formulation will be highlighted throughout this text.

To evaluate the integral terms in Eq. 3 each body is approximated as  $M_k$ -number of linear segments called panels, shown for a general element in Fig (7a). The ends of the panels coincides with the surface of the original body so that as  $M_k \rightarrow \infty$ , the original shape is recovered.  $M_k$ -number of panels leads to the body being approximated by  $M_k + 1$  boundary points. The integral in Eq. (3) now reduces to the sum of the integrated influence along each panel representing the body. The vortex sheets are now placed along straight paths between the start- and end-points of each panel. Defining a local panel coordinate system  $(x^*, z^*)$ , where the  $x^*$  axis coincides with the panel, as shown in Fig. 7b, the streamfunction contribution from the  $j$ -th panel is then the contribution of the infinitesimal segment  $dx_0$  located at  $x_0$  integrated from  $x_j^*$  to  $x_{j+1}^*$

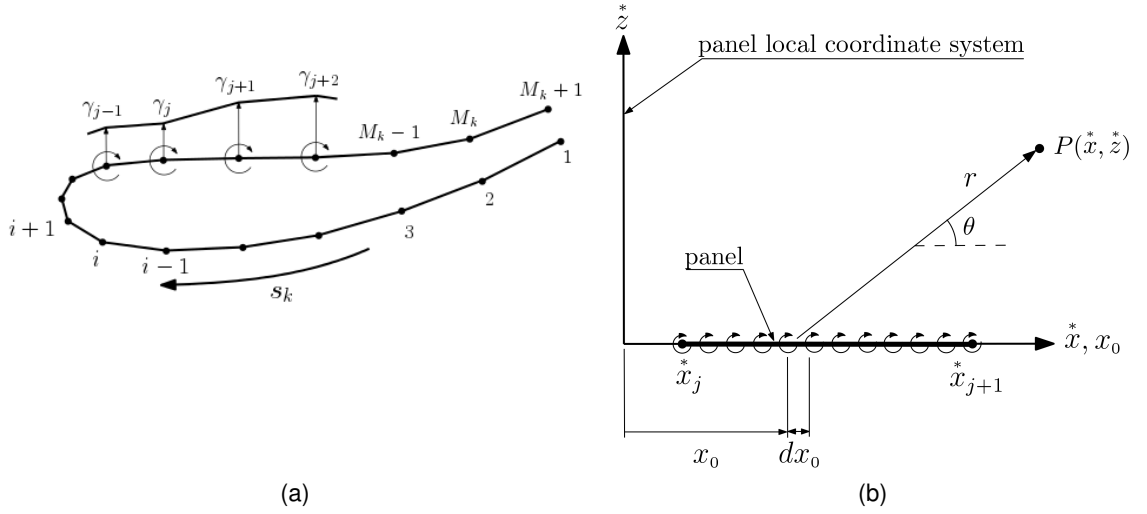


**Fig. 7 (a) A general element in the section approximated by panels with a linearly varying vortex distribution. (b) Nomenclature for calculating the streamfunction influence of a panel at a point  $P(x^*, z^*)$ .**

$$\Psi(x, z) = U_\infty(z \cos \alpha - x \sin \alpha) + \frac{1}{2\pi} \sum_{k=1}^N \sum_{j=1}^{M_k} \int_{x_j^*}^{x_{j+1}^*} \gamma(x_0) \ln r(x_0, x^*, z^*) dx_0, \quad (4)$$

where  $r = \sqrt{(x^* - x_0)^2 + z^{*2}}$ , since the local panel coordinate system is defined so that  $z_0 = 0$ .

The distribution  $\gamma(x_0)$  is chosen to vary linearly along each panel and is thus defined by its start and end values  $\gamma_j$ ,  $\gamma_{j+1}$ , as shown in Fig. 8. A linear variation is chosen to avoid discontinuities in  $\gamma$  at the panel boundary points, as a continuous distribution is required to allow the boundary condition to be applied at these points, as will be seen later. A continuous distribution is also preferred in multi-body cases to avoid problems with geometries that have small slotgaps [16, 18].

To evaluate the integral in Eq. (4),  $\gamma(x_0)$  is decomposed into a superposition of its mean value and a linear variation with zero mean, as seen in Fig. 9

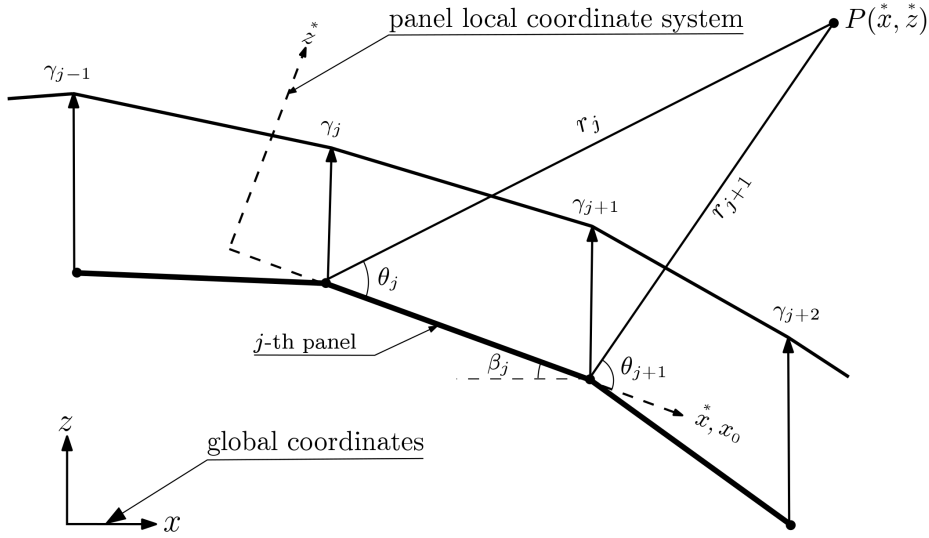


**Fig. 8 Detailed nomenclature for expressing the streamfunction influence of a single panel with linearly varying strength at a point  $P(x^*, z^*)$ .**

$$\begin{aligned}
 \gamma(x_0) &= \bar{\gamma} + \gamma'(x_0), \\
 \bar{\gamma} &= \frac{\gamma_{j+1} + \gamma_j}{2}, \\
 \gamma'(x_0) &= \frac{\gamma_{j+1} - \gamma_j}{x_{j+1}^* - x_j^*} (x_0^* - x_j^*) - \frac{\gamma_{j+1} - \gamma_j}{2}.
 \end{aligned} \tag{5}$$

Using this expression for  $\gamma(x_0)$ , Eq. (4) evaluates to

$$\Psi(x, z) = U_\infty (z \cos \alpha - x \sin \alpha) + \frac{1}{4\pi} \sum_{k=1}^N \sum_{j=1}^{M_k} [(\gamma_{j+1} + \gamma_j) {}^1\hat{\Psi}_j + (\gamma_{j+1} - \gamma_j) {}^2\hat{\Psi}_j], \tag{6}$$

where  ${}^1\hat{\Psi}_j$  represents the streamfunction contribution per unit strength of  $\gamma_{j+1} + \gamma_j$ ,  ${}^2\hat{\Psi}_j$  the contribution per unit strength of  $\gamma_{j+1} - \gamma_j$ , and are defined solely by the geometrical parameters defined in Fig. 8

$${}^1\hat{\Psi}_j = x^* \ln r_j - (x^* - x_{j+1}^*) \ln r_{j+1} - x_{j+1}^* (\theta_{j+1} - \theta_j), \tag{7}$$

$${}^2\hat{\Psi}_j = \left[ (2x^* - x_{j+1}^*) {}^1\hat{\Psi}_j + r_{j+1}^2 \ln r_{j+1} - r_j^2 \ln r_j + \frac{x^{*2} - (x^* - x_{j+1}^*)^2}{2} \right] \frac{1}{x_{j+1}^*}. \tag{8}$$

Here local panel coordinate system is chosen so its origin coincides with the panel start point, hence  $x_j^* = 0$ , which simplifies the expressions for  ${}^1\hat{\Psi}_j$  and  ${}^2\hat{\Psi}_j$ . These expressions are similar to what is presented in [8], but not identical due to differences in how distances

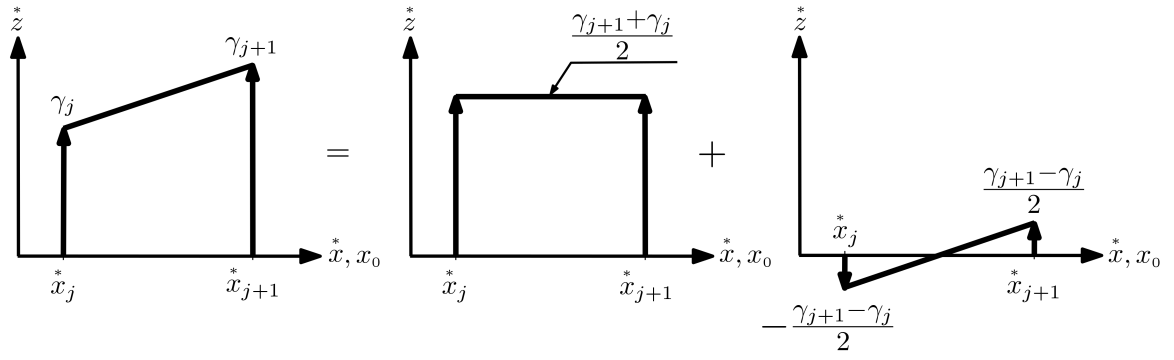


**Fig. 9** Decomposition of a vortex distribution of linearly varying strength into a superposition of its mean strength and a linearly varying distribution with a zero mean.

and angles are defined.

Since  ${}^1\hat{\Psi}_j$  and  ${}^2\hat{\Psi}_j$  are expressed in the local reference frame of the  $j$ -th panel, the geometry of the section needs to be transformed from global coordinates to local panel coordinates by the transformation

$$\begin{aligned} x^* &= (x - x_j) \cos \beta_j + (z - z_j) \sin \beta_j, \\ z^* &= -(x - x_j) \sin \beta_j + (z - z_j) \cos \beta_j, \\ x_{j+1}^* &= (x_{j+1} - x_j) \cos \beta_j + (z_{j+1} - z_j) \sin \beta_j, \end{aligned} \quad (9)$$

where  $\beta_j$  is the orientation of the  $j$ -th panel defined in Fig. 8. Figure 8 also shows the  $j$ -th boundary point to be the start point of the  $j$ -th panel and the end point of the  $(j - 1)$ -th panel. Collecting all terms containing  $\gamma_j$  in the summation of Eq. (6) therefore gives the influence per unit strength of  $\gamma_j$  at  $(x_i, z_i)$

$$\Psi(x_i, z_i) = U_\infty(z_i \cos \alpha - x_i \sin \alpha) + \sum_{k=1}^N \sum_{j=1}^{M_k+1} (a_{ij} \gamma_j)_k, \quad (10)$$

where  $a_{ij}$  is defined as the unit influence coefficient of  $\gamma_j$ , obtained by evaluating  ${}^1\hat{\Psi}_j$  and  ${}^2\hat{\Psi}_j$  at  $(x_i, z_i)$

$$a_{ij} = \frac{1}{4\pi} \left[ ({}^1\hat{\Psi}_j - {}^2\hat{\Psi}_j) + ({}^1\hat{\Psi}_{j-1} + {}^2\hat{\Psi}_{j-1}) \right]. \quad (11)$$

The boundary condition is applied by requiring the streamfunction to take constant values  $\Psi_k$  at the boundary points  $(x_i, z_i)$  of each body. Using this condition gives the general system for  $N$ -bodies

$$\sum_{k_j=1}^N \sum_{j=1}^{M_{k_j}+1} (a_{ij} \gamma_j)_{k_i k_j} - \Psi_{k_i} = U_\infty(x_i \sin \alpha - z_i \cos \alpha) \quad ; \quad 1 \leq i \leq M_{k_i}+1, \quad 1 \leq k_i \leq N, \quad (12)$$

where  $k_i$  and  $k_j$  represents the index of the body where the  $i$ -th and  $j$ -th boundary points, currently being considered, lie on respectively. Hence  $k_i = k_j$  indicates the influence of the body on itself being considered. Equations. (12) is a linear system of  $M_k + 1$  equations, with  $M_k + 1$  unknown  $\gamma_j$  values, and one unknown streamfunction value  $\Psi_k$  per body, and thus needs one additional relation per body to close the system. This is achieved by applying the Kutta-condition, specifying no aerodynamic load at each trailing edge

$$\gamma_1 + \gamma_{M_k+1} = 0 \quad ; \quad 1 \leq k \leq N, \quad (13)$$

results in a  $(M_k + 2) \times (M_k + 2)$  system per body.

Applying the boundary condition at the panel boundary points is not standard for panel methods, more common is using the panel mid-points. Here the former approach is required to obtain a closed system, since the value of  $\Psi_k$  can not be chosen arbitrarily in a multi-body case, where the relative streamfunction values on the surface of each body have physical meaning, representing the massflow passing between the bodies. This leads to one additional unknown per body and thus requires one additional relationship per body, which is obtained by applying the boundary condition at  $M_k + 1$  panel boundary points, as opposed to  $M_k$  panel mid-points. This highlights why a linear  $\gamma$  distribution is chosen, as a constant  $\gamma$  strength on each panel would lead to discontinuities in  $\gamma$  at the panel boundary points, causing Eq. (7) and (8) to become singular when  $k_i = k_j, i = j$  or  $k_i = k_j, i = j - 1$  in Eqs. (12).

The principal values of  $^1\hat{\Psi}_j$  and  $^2\hat{\Psi}_j$  still needs to be evaluated as special cases when  $k_i = k_j, i = j$  or  $k_i = k_j, i = j - 1$ , for the current formulation since  $r_j \rightarrow 0$  and  $r_{j+1} \rightarrow 0$  for these cases respectively. If a trailing edge is sharp i.e. points  $i = 1$  and  $i = M_k + 1$  coincide similar considerations need to be applied when  $k_i = k_j, i = 0, j = M_k$  and  $k_i = k_j, i = M_k + 1, j = 0$ .

One further difficulty arises when a trailing edge is sharp. Since the first and last boundary points for the body will coincide in this case, the first and last equation for this body in Eqs. (12) will be identical, and the system singular. To handle this the last equation for the body is replaced by an extrapolation of the  $\gamma$  values near its trailing edge

$$\gamma_1 - 2\gamma_2 + \gamma_3 - \gamma_{M-1} + 2\gamma_M - \gamma_{M+1} = 0 \quad , \quad (14)$$

this is identical to the way of handling these cases introduced in [28], which was later also adopted by Xfoil [8].

Eqs. (12) and Eqs. (13) from final system structured as

$$\begin{bmatrix} \begin{bmatrix} A_{1,1} \end{bmatrix} \\ \begin{bmatrix} A_{2,1} \end{bmatrix} \\ \vdots \\ \begin{bmatrix} A_{N,1} \end{bmatrix} \end{bmatrix} \begin{bmatrix} \begin{bmatrix} A_{1,2} \end{bmatrix} \\ \begin{bmatrix} A_{2,2} \end{bmatrix} \\ \ddots \\ \begin{bmatrix} A_{N,2} \end{bmatrix} \end{bmatrix} \cdots \begin{bmatrix} \begin{bmatrix} A_{1,N} \end{bmatrix} \\ \begin{bmatrix} A_{2,N} \end{bmatrix} \\ \vdots \\ \begin{bmatrix} A_{N,N} \end{bmatrix} \end{bmatrix} \begin{bmatrix} \gamma_1 \\ \gamma_2 \\ \vdots \\ \gamma_N \end{bmatrix} \begin{bmatrix} \mathbf{RHS}_1 \\ \mathbf{RHS}_2 \\ \vdots \\ \mathbf{RHS}_N \end{bmatrix} = \begin{bmatrix} \mathbf{RHS}_1 \\ \mathbf{RHS}_2 \\ \vdots \\ \mathbf{RHS}_N \end{bmatrix}, \quad (15)$$

where the sub-matrix  $A_{k_i,k_j}$  contains the streamfunction influence coefficients on the  $k_i$ -th body by the  $k_j$ -th body calculated using Eq. (11). When  $k_i = k_j$  the bodies influence on itself is calculated and the sub-matrix will include entries for  $\Psi_k$  and the Kutta-condition

$$A_{k_i,k_j} = \begin{bmatrix} a_{11} & a_{12} & \cdots & a_{1,M_k+1} & -1 \\ a_{21} & a_{22} & \cdots & a_{2,M_k+1} & -1 \\ \vdots & \vdots & \ddots & \vdots & \vdots \\ a_{M_k+1,1} & a_{M_k+1,2} & \cdots & a_{M_k+1,M_k+1} & -1 \\ 1 & 0 & \cdots & 1 & 0 \end{bmatrix} \quad \text{if } k_i = k_j, \quad (16)$$

$$A_{k_i,k_j} = \begin{bmatrix} a_{11} & a_{12} & \cdots & a_{1,M_k+1} & 0 \\ a_{21} & a_{22} & \cdots & a_{2,M_k+1} & 0 \\ \vdots & \vdots & \ddots & \vdots & \vdots \\ a_{M_k+1,1} & a_{M_k+1,2} & \cdots & a_{M_k+1,M_k+1} & 0 \\ 0 & 0 & \cdots & 0 & 0 \end{bmatrix} \quad \text{if } k_i \neq k_j. \quad (17)$$

$\gamma_k$  is the sub-vector of unknowns for the  $k$ -th body including the unknown  $\gamma_i$  values at the panel boundary points and the bodies unknown streamfunction value  $\Psi_k$

$$\gamma_k = \begin{bmatrix} \gamma_1 \\ \gamma_2 \\ \vdots \\ \gamma_{M_k+1} \\ \Psi_k \end{bmatrix}, \quad (18)$$

and  $\mathbf{RHS}_k$  is the vector of the freestream streamfunction contribution evaluated at each node of the  $k$ -th body using the right-hand-side (RHS) of Eq. (12)



$$\mathbf{RHS}_k = \begin{bmatrix} \Psi_{\infty_1} \\ \Psi_{\infty_2} \\ \vdots \\ \Psi_{\infty_{M_k+1}} \\ 0 \end{bmatrix}, \quad (19)$$

where the bottom entry is the RHS in Eq. (13). For a section consisting of  $K$ -elements accounting for ground effect, resulting in a total of  $N$ -bodies, where each body is approximated by  $M$ -panels, Eqs. (15) forms a  $N(M+2) \times N(M+2)$  linear system which can be solved for  $N(M+1)$  unknown  $\gamma_i$  values and  $N$  unknown  $\Psi_k$  values using Gaussian elimination.

## 4.2 Post Processing

Surface quantities are calculated by applying the definition of circulation as the line integral of velocity around a closed path  $A$

$$\Gamma = \oint_A \vec{V} \cdot d\vec{S}, \quad (20)$$

letting the path enclose an infinitesimal region of a vortex sheet with strength per unit length  $\gamma(s)$ , as shown in Fig. 10, the total circulation around the path equals the circulation of the infinitesimal region of the vortex sheet  $\gamma(s)ds$

$$\Gamma = \gamma(s)ds = (q_{t1} - q_{t2})ds + (q_{n1} - q_{n2})dn. \quad (21)$$

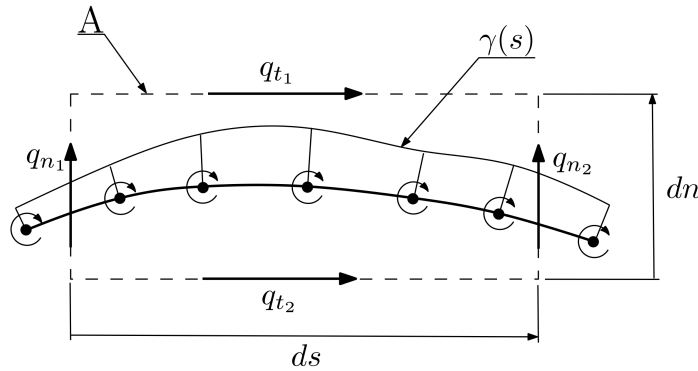


**Fig. 10 Circulation around the path  $A$  enclosing an infinitesimal segment of a vortex sheet placed along the path  $s$ .**

As  $dn \rightarrow 0$ , the circulation around the path approaches the difference in tangential velocity between the top and the bottom of the vortex sheet,  $(q_{t1} - q_{t2})ds$ . Since the vortex sheets placed on the surface of the wing-section elements form a closed path, the flow inside this path is stagnant  $q_{t2} = 0$ , and the local circulation of the vortex sheet is equal to the surface tangential velocity  $\gamma(s) = q_{t1}$ . The surface pressure coefficient is then obtained through the Bernoulli principle as a simple relation to the local  $\gamma_i$  value at each boundary point, where  $\gamma_i$  is obtained directly by the solution of the analysis problem

$$C_{P_i} = 1 - \left( \frac{\gamma_i}{U_\infty} \right)^2. \quad (22)$$

Having a formulation of the analysis problem that allows a simple relation between the unknowns in the governing equations (12), and  $C_P$ , is essential to simplify the design method formulation, since it allows  $\gamma_i$  to be directly specified using the sought pressure distribution through applying Eq. (22).

The lift coefficient is calculated by considering the path  $A$  as enclosing an element in the section, as shown in Fig. 11. Letting the path  $A$  approach the surface of the elements panelled geometry, the integral in Eq. (20) reduces to the sum of the integrated tangential velocities over each panel, which for a linear distribution is obtained from the average tangential velocity along the panel  $\bar{q}_i$ , and the panel-length  $\delta s_i$ . The total lift coefficient of the section is then the sum of the contributions of each individual element

$$C_{L_k} = \frac{1}{U_\infty c_k} \sum_{i=1}^{M_k} \bar{q}_i \delta s_i, \quad (23)$$

$$C_{L_{tot}} = \sum_{k=1}^K C_{L_k}, \quad (24)$$

where  $\bar{q}_i$  is obtained from the average  $\gamma$ -value on the panel as  $\bar{q}_i = \bar{\gamma}_i = (\gamma_i + \gamma_{i+1})/2$ , using Eq. (22).  $\delta s_i$  is simply  $x_{j+1}^*$  evaluated in the local coordinate system of that panel, already available from the unit influence coefficient calculations. The element chord  $c_k$ , is taken as unit length, since the chord length to use for normalisation is ambiguous in a multi-element case. Since purely potential-flow is considered, there is no dependency of  $C_{L_k}$  on  $U_\infty$ , which is taken as  $U_\infty = 1$  for simplicity. The lift coefficient for an element is then twice the circulation of the element, and will scale with the chord length of the input geometry.

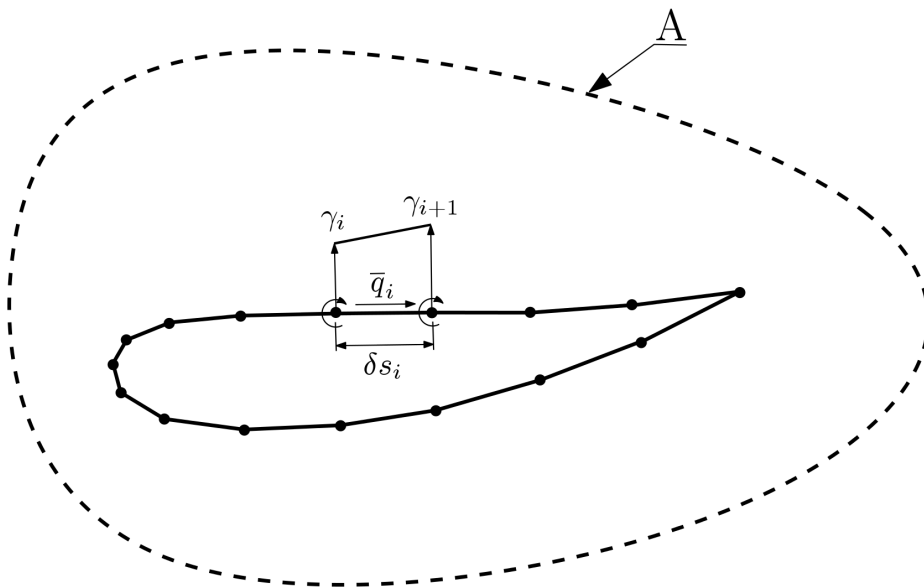


**Fig. 11** Circulation around the path  $A$  enclosing a single element in the section.

By discretising the field surrounding the geometry into a  $N_x \times N_z$  grid, field quantities can be calculated by considering the influence of the known surface vorticity of the geometry at each point on the grid. To plot streamlines the governing equation (10) for the streamfunction value is applied on the grid

$$\Psi(x_i, z_i) = U_\infty(z_i \cos \alpha - x_i \sin \alpha) + \sum_{k=1}^N \sum_{j=1}^{M_k+1} (a_{ij} \gamma_j)_k \quad ; \quad 1 \leq i \leq N_x \times N_z, \quad (25)$$

the grid can then be interpolated to find lines of  $\Psi = \text{const.}$  to produce streamlines. To find stagnation streamlines, the grid is interpolated for the known values of the streamfunction on the surface of the elements  $\Psi_k$ , obtained from the solution of the analysis problem.

In the field the simple relation of Eq. (22) can not be applied. To evaluate  $C_p$  on the grid, the velocity at each field point needs to be evaluated as the sum of the influence from each panel, calculated from the definition of velocity potential

$$u = \frac{\partial \Phi}{\partial x} \quad w = \frac{\partial \Phi}{\partial z}. \quad (26)$$

The general expression for the velocity components at a point is obtained by differentiation of the expression equivalent to Eq. (4) for the velocity potential

$$u(x, z) = U_\infty \cos \alpha - \frac{1}{2\pi} \sum_{k=1}^N \sum_{j=1}^{M_k} \int_{x_j^*}^{x_{j+1}^*} \gamma(x_0) \frac{\partial \theta}{\partial x}(x_0, x^*, z^*) dx_0, \quad (27)$$

$$w(x, z) = U_\infty \sin \alpha - \frac{1}{2\pi} \sum_{k=1}^N \sum_{j=1}^{M_k} \int_{x_j^*}^{x_{j+1}^*} \gamma(x_0) \frac{\partial \theta}{\partial z}(x_0, x^*, z^*) dx_0, \quad (28)$$

where derivatives of  $\theta$  is obtained from its definition,  $\theta = \tan^{-1} \left( \frac{z^*}{x^* - x_0} \right)$

$$\frac{\partial \theta}{\partial x} = -\frac{z^*}{(x^* - x_0)^2 + z^{*2}} \quad \frac{\partial \theta}{\partial z} = \frac{x^* - x_0}{(x^* - x_0)^2 + z^{*2}}. \quad (29)$$

Evaluating Eq. (27) and Eq. (28) for the  $\gamma(x_0)$  distribution defined in Eqs. (5), and applying them to the  $N_x \times N_z$  grid, gives a grid that can be interpolated for velocity

$$u(x_i, z_i) = U_\infty \cos \alpha + \sum_{k=1}^N \sum_{j=1}^{M_k+1} (u_{ij} \gamma_j)_k \quad ; \quad 1 \leq i \leq N_x \times N_z, \quad (30)$$

$$w(x_i, z_i) = U_\infty \sin \alpha + \sum_{k=1}^N \sum_{j=1}^{M_k+1} (w_{ij} \gamma_j)_k \quad ; \quad 1 \leq i \leq N_x \times N_z, \quad (31)$$

where similarly to previously,  $w_{ij}$  is the  $x$ -velocity unit influence coefficient, and  $w_{ij}$  the  $z$ -velocity unit influence coefficient of  $\gamma_j$  at  $(x_i, z_i)$ . Here a coordinate transformation is applied to obtain the unit influence coefficients in the global coordinate system, since velocity is a vector quantity

$$u_{ij} = u_{ij}^* \cos \beta_j + w_{ij}^* \sin \beta_j, \quad (32)$$

$$w_{ij} = w_{ij}^* \cos \beta_j - u_{ij}^* \sin \beta_j, \quad (33)$$

where  $u_{ij}^*, w_{ij}^*$  are the unit influence coefficients in local panel coordinates

$$u_{ij}^* = \frac{1}{4\pi} \left[ ({}^1\hat{U}_j - {}^2\hat{U}_j) + ({}^1\hat{U}_{j-1} + {}^2\hat{U}_{j-1}) \right] \quad (34)$$

$$w_{ij}^* = \frac{1}{4\pi} \left[ ({}^1\hat{W}_j - {}^2\hat{W}_j) + ({}^1\hat{W}_{j-1} + {}^2\hat{W}_{j-1}) \right] \quad (35)$$

defined solely by geometrical parameters through  ${}^1\hat{U}_j$ , representing the  $x$ -velocity contribution per unit strength of  $\gamma_{j+1} + \gamma_j$ ,  ${}^2\hat{U}_j$  representing the  $x$ -velocity contribution per unit strength of  $\gamma_{j+1} - \gamma_j$ ,  ${}^1\hat{W}_j$  representing the  $z$ -velocity contribution per unit strength of  $\gamma_{j+1} + \gamma_j$ , and  ${}^2\hat{W}_j$  representing the  $z$ -velocity contribution per unit strength of  $\gamma_{j+1} - \gamma_j$

$${}^1\hat{U}_j = \theta_{j+1} - \theta_j, \quad (36)$$

$${}^2\hat{U}_j = \left[ \left( 2x^* - x_{j+1}^* \right) {}^1\hat{U}_j + 2z^* \ln \frac{r_{j+1}}{r_j} \right] \frac{1}{x_{j+1}^*}, \quad (37)$$

$${}^1\hat{W}_j = \ln \frac{r_{j+1}}{r_j}, \quad (38)$$

$${}^2\hat{W}_j = \left[ \left( 2x^* - x_{j+1}^* \right) {}^1\hat{W}_j - 2z^* (\theta_{j+1} - \theta_j) + 2x_{j+1}^* \right] \frac{1}{x_{j+1}^*}. \quad (39)$$

Here both  ${}^2\hat{U}_j$  and  ${}^1\hat{W}_j$  have logarithmic singularities if the point  $(x^*, z^*)$  would coincide with a panel boundary point, which together with the additional transformation needed that would complicate calculating derivatives of these expressions as needed in the design method, means a velocity based formulation would be unsuitable for use in solving the analysis problem.

The pressure coefficient in the field is then calculated from the local velocity magnitude

$$C_{P_i} = 1 - \frac{u_i^2 + w_i^2}{U_\infty^2}. \quad (40)$$

### 4.3 Potential-Flow Design Method

The design method is based on the same governing equations for the streamfunction constraint (12), and the Kutta condition (13), presented in Section 4.1. Instead of solving for  $\gamma_i$  on the surface of each body, such that the bodies becomes streamlines in the flow field,  $\gamma_i$  is instead specified over design segments  $i_{S_k} \leq i \leq i_{E_k} ; 1 \leq k \leq N$ , where the positions of the panel boundary points are instead considered the unknowns, as shown in Fig. 12. The solution is then found by altering the geometry to satisfy the governing equations for the specified  $\gamma_i$ , calculated from the sought  $C_P$ -distribution using Eq. (22).  $\gamma_i$  is always specified to be symmetrical about the mirror-plane to ensure the section and its mirror retains symmetry about  $z = 0$  when the geometry is altered.

For boundary points outside of the design segments,  $i < i_{S_k} ; 1 \leq k \leq N$  and  $i > i_{E_k} ; 1 \leq k \leq N$ , the unknown remains the  $\gamma_i$  value. This method of restricting the geometry change to pre-defined segments is preferred for the design problems targeted by this tool since the designer retains control over the geometrical envelope which is strictly regulated [1].

Positions of the boundary points are defined by their coordinates  $(x_i, z_i)$ , hence for each point  $i_{S_k} \leq i \leq i_{E_k} ; 1 \leq k \leq N$ , there are two unknowns in Eq. (12), leading to a total number of  $M_k + 3 + (i_{E_k} - i_{S_k})$  unknowns per body. Equations (12) and (13) provides  $M_k + 2$  equations per body, and the system needs to be closed by additional relations. This is done by specifying an allowed direction of motion for the solution, as a vector passing through the original coordinate of a boundary point, with a direction normal to the original surface. The normal is used as it allows large movements without boundary points crossing paths, which avoids  $^2\hat{\Psi}_j$  approaching singularity.

The normal direction at  $i$  is calculated as the average normal direction of the adjacent panels on the original body as shown in Fig. 13a. Panel normal direction are calculated as the negative reciprocal of the panel slope

$$\delta x_1 = x_i - x_{i-1} \quad \delta z_1 = z_i - z_{i-1} , \quad (41)$$

$$\delta x_2 = x_{i+1} - x_i \quad \delta z_2 = z_{i+1} - z_i , \quad (42)$$

and the adjacent panel normal directions  $n_1, n_2$

$$n_1 = (-\delta z_1, \delta x_1) \quad n_2 = (-\delta z_2, \delta x_2) , \quad (43)$$

The normal at  $i$  is then the average direction of  $n_1$  and  $n_2$ , here normalised to unit length

$$\hat{n}_i = \frac{((z_{i-1} - z_{i+1}), (x_{i+1} - x_{i-1}))}{\sqrt{(z_{i-1} - z_{i+1})^2 + (x_{i+1} - x_{i-1})^2}} . \quad (44)$$



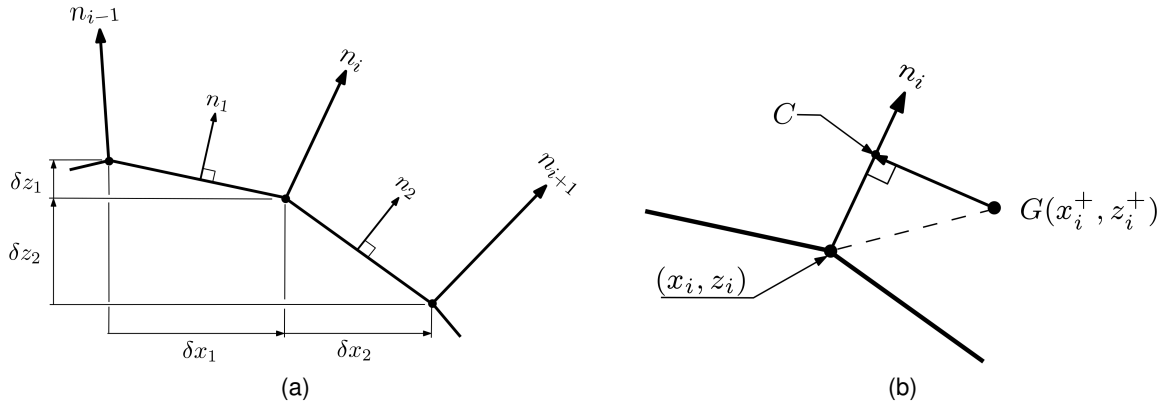


**Fig. 13 (a) Nomenclature for calculating the surface normal direction at  $i$ . (b) Surface normal direction with a prospective solution  $G(x_i^+, z_i^+)$  for the new position of the boundary point originally located at  $(x_i, z_i)$ .**

The solution is constrained to this direction by considering point  $G(x_i^+, z_i^+)$ , a prospective solution for the new position of the boundary point originally located at  $(x_i, z_i)$ , as shown in Fig. 13b.  $C$  is the point on  $\hat{n}_i$  of shortest distance to  $G$ , the vector  $\overrightarrow{GC}$  is then normal to  $\hat{n}_i$ , and by definition of the dot-product,  $\overrightarrow{GC} \cdot \hat{n}_i = 0$ . The direction of  $\hat{n}_i$  is  $(n_{i_x}, n_{i_z})$ , and the vector in this direction passing through  $(x_i, z_i)$  is parameterised as  $(x_i, z_i) + t(n_{i_x}, n_{i_z})$ , for  $-\infty \leq t \leq \infty$ . Hence the coordinates of  $C$

$$C = ((x_i + tn_{i_x}), (z_i + tn_{i_z})), \quad (45)$$

for some  $t$ , found by applying the condition  $\overrightarrow{GC} \cdot \hat{n}_i = 0$

$$t = \frac{n_{i_x}(x_i^+ - x_i) + n_{i_z}(z_i^+ - z_i)}{n_{i_x}^2 + n_{i_z}^2}. \quad (46)$$

By requiring  $|\overrightarrow{GC}| = 0$ , the movement of the solution is ensured to be compatible with the direction  $\hat{n}_i$ . This condition is enforced for boundary points  $i_{S_k} < i < i_{E_k}$ ;  $1 \leq k \leq N$ , while at the end-points of each design segment  $i = i_{S_k}$ ;  $1 \leq k \leq N$ , and  $i = i_{E_k}$ ;  $1 \leq k \leq N$ , no movement is specified to ensure continuity of the bodies profile at the points where the design segment meets the fixed part of the geometry

$$|\overrightarrow{GC}|_i = \sqrt{(x_i - x_i^+ + tn_{i_x})^2 + (z_i - z_i^+ + tn_{i_z})^2} = 0 \quad ; \quad i_{S_k} < i < i_{E_k}, \quad 1 \leq k \leq N, \quad (47)$$

$$x_{i_{S_k}} - x_{i_{S_k}}^+ = 0 \quad ; \quad 1 \leq k \leq N, \quad (48)$$

$$z_{i_{S_k}} - z_{i_{S_k}}^+ = 0 \quad ; \quad 1 \leq k \leq N, \quad (49)$$

$$x_{i_{E_k}} - x_{i_{E_k}}^+ = 0 \quad ; \quad 1 \leq k \leq N, \quad (50)$$

$$z_{i_{E_k}} - z_{i_{E_k}}^+ = 0 \quad ; \quad 1 \leq k \leq N. \quad (51)$$

Specifying a reasonable direction of motion for the solution is necessary, not only to close the system of equations, but also to avoid trivial solutions that could otherwise exist where

the boundary points are moved along the original surface, to a position where the specified pressure distribution is satisfied, effectively leading to a solution where the profile of the body remains identical, and only the distribution of the boundary points is changed.

By applying Eqs. (47-51) the system now contains  $M_k + 5 + (i_{E_k} - i_{S_k})$  equations per body, which allows an addition of two variables for each body. These are introduced as function modes to the specified pressure distribution, in the form of two quadratic shape-functions weighted by constants  $A_k, B_k$

$$\gamma_i = \gamma_{sp_i} + A_k g(x_i) + B_k h(x_i) \quad ; \quad i_{S_k} \leq i \leq i_{E_k}, \quad 1 \leq k \leq N, \quad (52)$$

where  $\gamma_{sp_i}$  is the user specified  $\gamma$  via the sought  $C_P$ -distribution using Eq. (22).  $g(x_i)$  and  $h(x_i)$  are defined as

$$g(x_i) = \left( \frac{x_{i_{E_k}} - x_i}{x_{i_{E_k}} - x_{i_{S_k}}} \right)^2 \quad ; \quad i_{S_k} \leq i \leq i_{E_k}, \quad 1 \leq k \leq N, \quad (53)$$

$$h(x_i) = \left( \frac{x_{i_{S_k}} - x_i}{x_{i_{S_k}} - x_{i_{E_k}}} \right)^2 \quad ; \quad i_{S_k} \leq i \leq i_{E_k}, \quad 1 \leq k \leq N, \quad (54)$$

which allows more freedom in the specified pressure distribution at the ends of the design segments, where they need to match the fixed part of the geometry.

This formulation is adapted from [8], which is in turn is adapted from [29]. These are applications of the Lighthill constraints [28], which defines the limitations on the pressure distributions achievable by a closed body.

Introducing two degrees of freedom is also beneficial from a practical standpoint, as it allows a “closest” solution to be found, even though the prescribed pressure distribution may not be physical, and would result in a discontinuous or non-smooth profile. This simplifies usage, as otherwise, the designer would have to always specify pressure distributions compatible with the fixed parts of the geometry. The effect these function modes has on the solution of a design problem is shown in section 6.3.

Considering the non-linear dependency on geometry of Equations (7), (8) and (47), the equation set is reformulated as the objective function  $\mathbf{F}(\mathbf{W})$ , which is to be minimised

$$\mathbf{F}(\mathbf{W}) = \begin{pmatrix} \mathbf{f}_1(\mathbf{w}_1) \\ \mathbf{f}_2(\mathbf{w}_2) \\ \vdots \\ \mathbf{f}_N(\mathbf{w}_N) \end{pmatrix}, \quad (55)$$

where the  $i$ -th entry of  $\mathbf{f}_k$  is  $f_i$ , and is given by the streamfunction constraints (12), the Kutta condition (13), the movement compatibility conditions (47), and the geometric continuity



conditions (48)-(51) for the  $k$ -th body

$$\begin{aligned}
 f_i &\equiv U_\infty(z_i \cos \alpha - x_i \sin \alpha) + \sum_{k=1}^N \sum_{j=1}^{M_k+1} (a_{ij} \gamma_j)_k - \Psi_k = 0 & ; 1 \leq i \leq M_k+1 \\
 f_{M_k+2} &\equiv \gamma_1 + \gamma_{M_k+1} = 0 \\
 f_{M_k+3} &\equiv x_{i_{S_k}} - x_{i_{S_k}}^+ = 0 \\
 f_{M_k+4} &\equiv z_{i_{S_k}} - z_{i_{S_k}}^+ = 0 \\
 f_{M_k+5} &\equiv x_{i_{E_k}} - x_{i_{E_k}}^+ = 0 \\
 f_{M_k+6} &\equiv z_{i_{E_k}} - z_{i_{E_k}}^+ = 0 \\
 f_{M_k+6-i_{S_k}+i} &\equiv |\mathbf{GC}|_i = 0 & ; i_{S_k} < i < i_{E_k}
 \end{aligned} \tag{56}$$

The  $i$ -th entry of  $\mathbf{w}_k$  is  $w_i$ , and is given by the unknown boundary point coordinates  $(x_i, z_i)$  in the design segment, the unknown  $\gamma_i$  for boundary points outside of the design segment,  $\Psi_k$ ,  $A_k$  and  $B_k$  for the  $k$ -th body.

To solve this system a combined Newton-Powell method is used. This is a modification of Powells' Hybrid method, as described in [30], where  $\mathbf{F}(\mathbf{W})$  is linearised about the current solution and the linearised systems residual minimised within a confidence region of the solution-step  $\mathbf{W}^+ - \mathbf{W}$ , using a line search method

$$\min. \{ \|\mathbf{J}(\mathbf{W}^+ - \mathbf{W}) + \mathbf{F}\| \} , \tag{57}$$

where  $\mathbf{J}$  is the Jacobian matrix. The allowed solution-step is limited to

$$\|\mathbf{D}(\mathbf{W}^+ - \mathbf{W})\| \leq \Delta , \tag{58}$$

where  $\Delta$  is a user determined positive number,  $\mathbf{D}$  a diagonal scaling matrix, both set by trial and error approach. When a solution vector  $\mathbf{W}^+$  has been found that produces a sufficient decrease in the residual of  $\mathbf{F}$ , the current solution is updated and the Jacobian matrix recalculated for the next iteration

$$\mathbf{W} \rightarrow \mathbf{W}^+ . \tag{59}$$

The iteration is repeated until the current solution produces a sufficiently small residual.

In linearising the system the Jacobian matrix  $\mathbf{J}$  needs to be evaluated, which involves differentiating  $f_i$  with respects to each  $w_i$ . This is for most part straightforward barring the summation term in Eq. (12), where the influence coefficient  $a_{ij}$ , depending on the expressions  $^1\hat{\Psi}_j, ^2\hat{\Psi}_j$ , ultimately needs to be differentiated. From Eq. (11)  $a_{ij}$  has the functional relationship  $a_{ij} = f(x_i, z_i, x_{j-1}, z_{j-1}, x_j, z_j, x_{j+1}, z_{j+1})$ , which for a general variable  $p$  in the summation term

$$\frac{\partial}{\partial p} (a_{ij}\gamma_j) = \gamma_j \frac{\partial a_{ij}}{\partial p} + a_{ij} \frac{\partial \gamma_j}{\partial p}, \quad (60)$$

where the  $\gamma_j$  derivative is obtained from differentiation of Eq. (52), and the  $a_{ij}$  derivative given by

$$\frac{\partial a_{ij}}{\partial p} = \frac{1}{4\pi} \left[ \left( \frac{\partial^1 \hat{\Psi}_j}{\partial p} - \frac{\partial^2 \hat{\Psi}_j}{\partial p} \right) + \left( \frac{\partial^1 \hat{\Psi}_{j-1}}{\partial p} + \frac{\partial^2 \hat{\Psi}_{j-1}}{\partial p} \right) \right], \quad (61)$$

and the chain rule is applied to obtain derivatives in the global coordinate system using the transformation in Eq. (9)

$$\frac{\partial^1 \hat{\Psi}_j}{\partial p} = \frac{\partial^1 \hat{\Psi}_j}{\partial x_i^*} \frac{\partial x_i^*}{\partial p} + \frac{\partial^1 \hat{\Psi}_j}{\partial z_i^*} \frac{\partial z_i^*}{\partial p} + \frac{\partial^2 \hat{\Psi}_j}{\partial x_{j+1}^*} \frac{\partial x_{j+1}^*}{\partial p}, \quad (62)$$

$$\frac{\partial^2 \hat{\Psi}_j}{\partial p} = \frac{\partial^2 \hat{\Psi}_j}{\partial x_i^*} \frac{\partial x_i^*}{\partial p} + \frac{\partial^2 \hat{\Psi}_j}{\partial z_i^*} \frac{\partial z_i^*}{\partial p} + \frac{\partial^2 \hat{\Psi}_j}{\partial x_{j+1}^*} \frac{\partial x_{j+1}^*}{\partial p}, \quad (63)$$

$$\frac{\partial^1 \hat{\Psi}_{j-1}}{\partial p} = \frac{\partial^1 \hat{\Psi}_{j-1}}{\partial x_i^*} \frac{\partial x_i^*}{\partial p} + \frac{\partial^1 \hat{\Psi}_{j-1}}{\partial z_i^*} \frac{\partial z_i^*}{\partial p} + \frac{\partial^1 \hat{\Psi}_{j-1}}{\partial x_{j+1}^*} \frac{\partial x_{j+1}^*}{\partial p}, \quad (64)$$

$$\frac{\partial^2 \hat{\Psi}_{j-1}}{\partial p} = \frac{\partial^2 \hat{\Psi}_{j-1}}{\partial x_i^*} \frac{\partial x_i^*}{\partial p} + \frac{\partial^2 \hat{\Psi}_{j-1}}{\partial z_i^*} \frac{\partial z_i^*}{\partial p} + \frac{\partial^2 \hat{\Psi}_{j-1}}{\partial x_{j+1}^*} \frac{\partial x_{j+1}^*}{\partial p}. \quad (65)$$

These Jacobian entries need to be calculated as increments, as each variable will occur in several instances of  $a_{ij}$ . For boundary points where the geometry is fixed, the unknown is  $\gamma_j$  and the Jacobian entry  $a_{ij}$ .

## 5 Validation

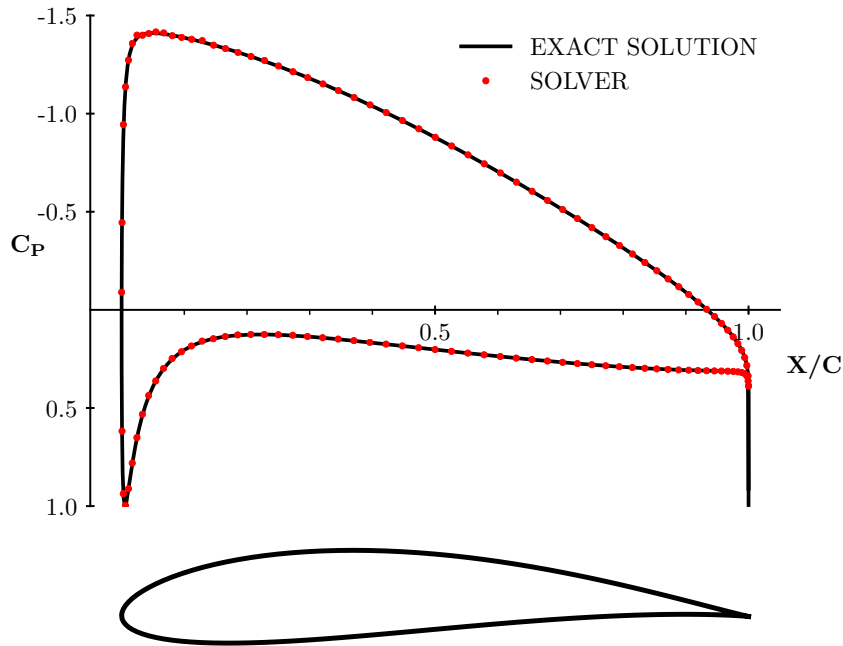
In this section the implementation of the analysis method is first validated against exact solutions from potential-flow theory or solutions from established panel codes. The implementation of the design method is then validated by cases where the prescribed pressure distributions correspond to already known geometries. All computations have been run on a standard Laptop-PC with an Intel Core i5-5200U 2.20 GHz CPU.

### 5.1 Analysis Validation

The cases in this section are meant to display the accuracy and computation requirements of the analysis methods implementation, starting with a simple single element case, progressing to ground effect and multi-element cases.

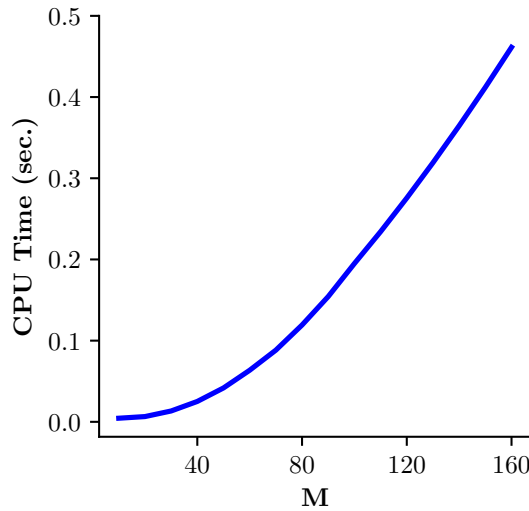
#### 5.1.1 Single Element Analysis Validation

Figure 14 shows the comparison of calculated and exact pressure distributions on a conformally mapped single-element airfoil at  $\alpha = 4$  deg. using  $M = 120$ . A good agreement is obtained. The exact results for this case were obtained by a Kármán–Trefftz transform.



**Fig. 14 Calculated and exact pressure distributions. Single element analysis validation case.**  $\alpha = 4$ ,  $M = 120$ .

Also shown are the computational requirements of this case for varying  $M$  in Fig. 15. Values for selected  $M$  are tabulated in Table 1, together with the error in  $C_L$ . The computational requirement is specified as the total CPU time required to import and panel the geometry, build and solve the equation system (15), and plotting the  $C_P$ . For simple cases like this one, results are obtained effectively immediately for any number of panels. The CPU time trend is approximately  $\propto M^2$ , suggesting that the main cost lies in building the system Eqs. (15).  $C_L$  error is defined as the difference between the exact value and the value obtained from Eq (24).



M	CPU Time (sec.)	$C_L$ Error
40	0.028	0.286%
80	0.122	0.078%
120	0.277	0.038%
160	0.461	0.025%

**Fig. 15** Computational requirements as a function of  $M$ . Single element analysis validation case.

**Table 1** Computational requirements and  $C_L$  error for selected  $M$ . Single element analysis validation case.

### 5.1.2 Ground Effect Analysis Validation

For validating ground effect implementation no exact solution is readily available. JavaFoil [9] is therefore used, which is an airfoil analysis tool capable of simulating wing-in-ground (WIG). The pressure distribution and  $C_L$  value the analysis method is compared to here is thus not exact values, and therefore labelled reference values, with the  $C_L$  comparison considered a difference rather than an error.

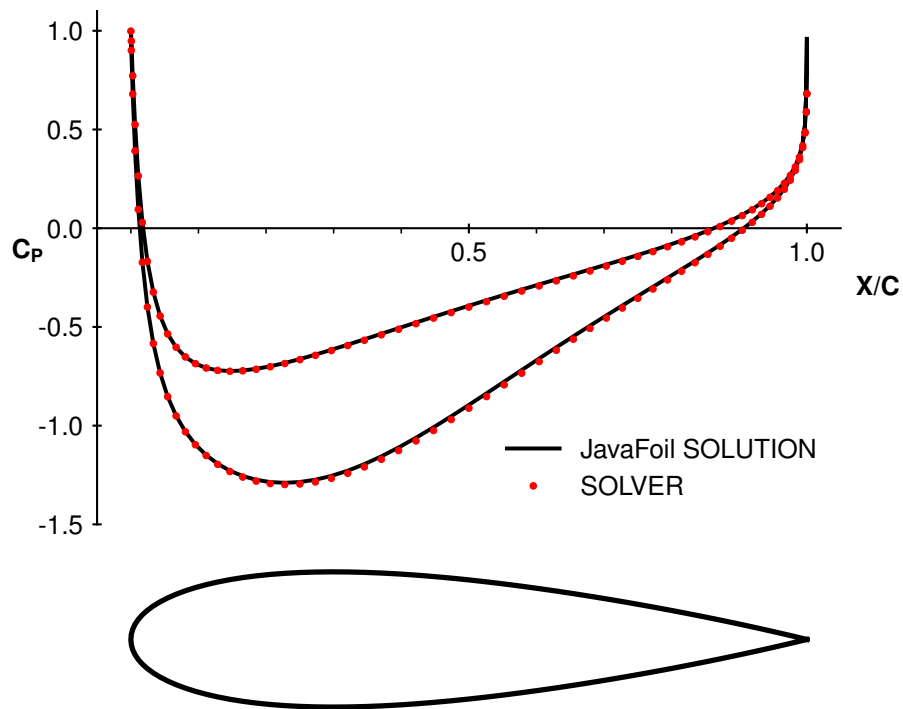


**Fig. 16** Calculated and reference pressure distributions. Ground effect analysis validation case.  $h/c = 0.2$ ,  $\alpha = 0$ ,  $M = 120$ .

The geometry for this case is a NACA 0020 at  $\alpha = 0$ , using  $M = 120$ . For the ground effect simulation  $h/c = 0.2$  is used, meaning the lowest point on the airfoil is 0.2 chord lengths away from the ground-plane. The calculated and reference pressure distributions for this case are shown in Fig. 16 and generally shows a good agreement. Some slight differences can be spotted towards the back of the airfoil, where the calculated  $C_P$  is slightly lower. Despite this difference, the  $C_L$  values are close as shown in Table 2. The  $C_L$  difference does not have the same convergence pattern as the previous case, likely due to the slight  $C_P$  differences on the two sides of the airfoils cancelling each other to varying degrees for different  $M$ . In Fig. 17 the cost of the simulation is shown to have increases by four compared to the previous case in free-flow, which is as expected when the number of unknown are doubled. Overall these results are considered satisfactory in terms of accuracy.

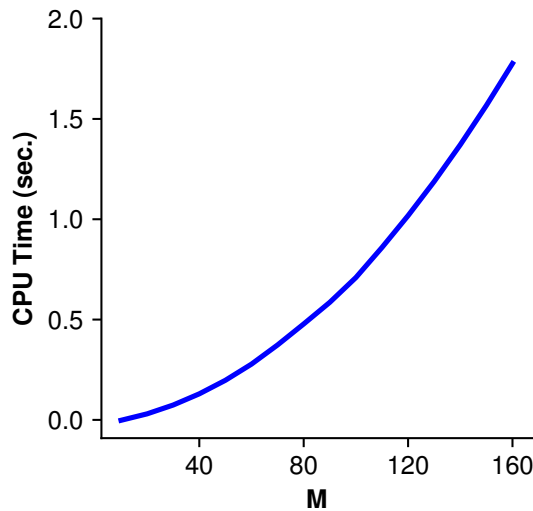


**Fig. 17 Computational requirements as a function of  $M$ . Ground effect analysis validation case.**

M	CPU Time (sec.)	$C_L$ Diff.
40	0.1	0.7%
80	0.5	0.3%
120	1.1	0.1%
160	1.9	0.07%

**Table 2 Computational requirements and  $C_L$  error for selected  $M$ . Ground effect analysis validation case.**

### 5.1.3 Multi-Element Analysis Validation

For the multi-element case an exact solution is again available. This solution is a four-element, conformally mapped wing section obtained from [31]. For this case  $\alpha = 0$ , and  $M = 120$ , meaning 120 panels are used for each element in the section, and the total number of panels in the calculation is  $K \times M = 480$ , with  $K = 4$  in this case. The comparison of calculated and exact pressure distribution for this case, presented in Fig. 18, shows good agreement. The inability to fully predict the TE stagnation-point is a result of the averaging of  $\gamma$ , used at the TE in Eq. (14).

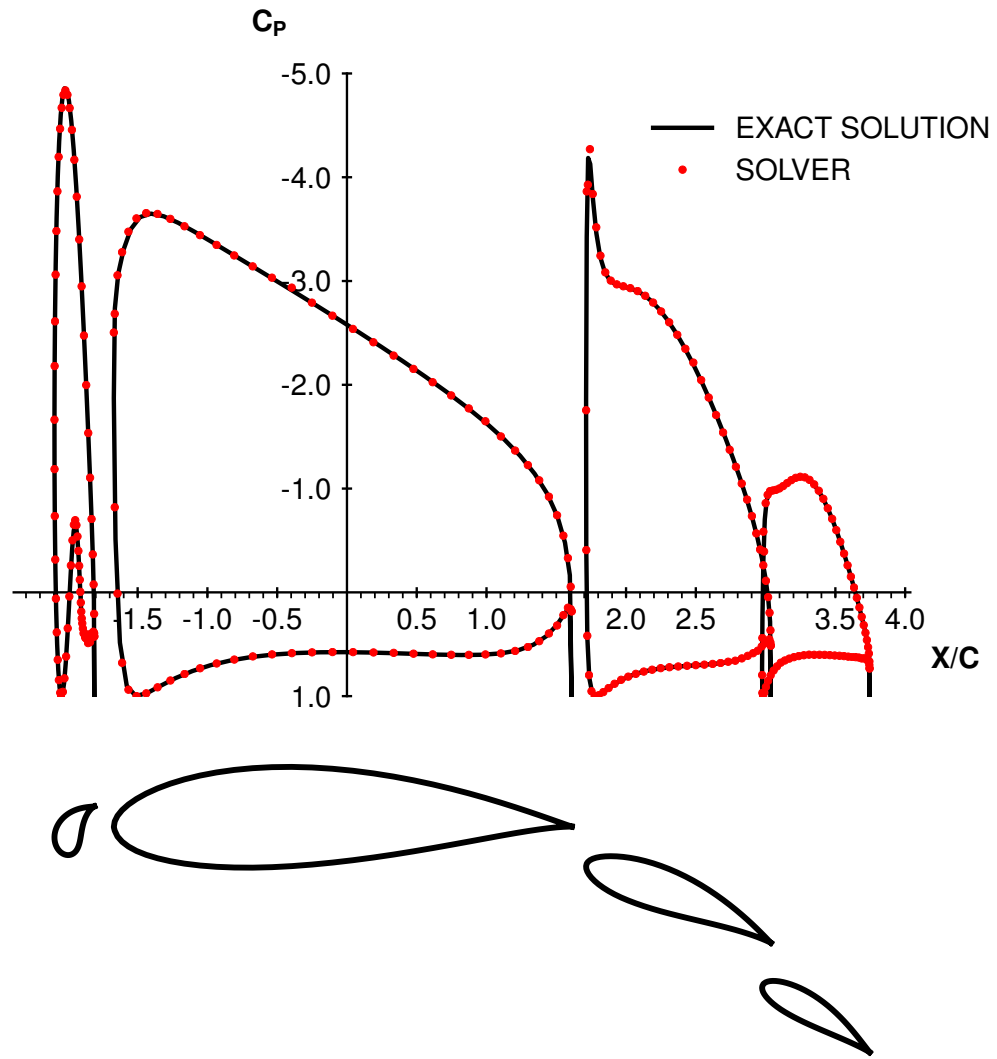


**Fig. 18** Calculated and exact pressure distributions. Multi-element analysis validation case.  $\alpha = 0$ ,  $M = 120$ .

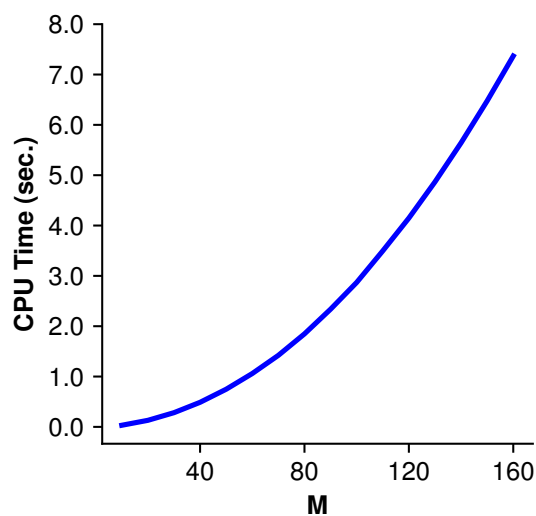


**Fig. 19** Computational requirements as a function of  $M$ . Multi-element analysis validation case.

$M$	CPU Time (sec.)	$C_L$ Error
40	0.5	4.4%
80	1.9	2.2%
120	4.1	1.8%
160	7.4	1.6%

**Table 3** Computational requirements and  $C_L$  error for selected  $M$ . Multi-element analysis validation case.

The computational requirements and  $C_L$  error for this case is shown in Figure. 19 and Table 3 respectively. The CPU time shows four elements are 16 times as costly calculate as the single element case.

## 5.2 Design Validation

The cases in this section are meant to display the accuracy and computation requirements of the design methods implementation, starting with a simple single element case, progressing to ground effect and multi-element cases.

For validating the design method, the pressure distribution of known geometries are used as a target  $C_P$ , this target distribution is then specified on a distorted version of the known geometry. The design method should then recover the known geometry as the solution to the design problem. For these cases the known geometry is taken as a NACA 0020, or a series of several NACA 0020, for simplicity. The distorted geometries are obtained by modifying one surface of the NACA 0020 to correspond to a NACA 0012. In these cases the specified pressure distribution will be compatible with the fixed part of the geometry and  $A_k$  and  $B_k$  can be set to zero in the solution.

### 5.2.1 Single Element Design Validation

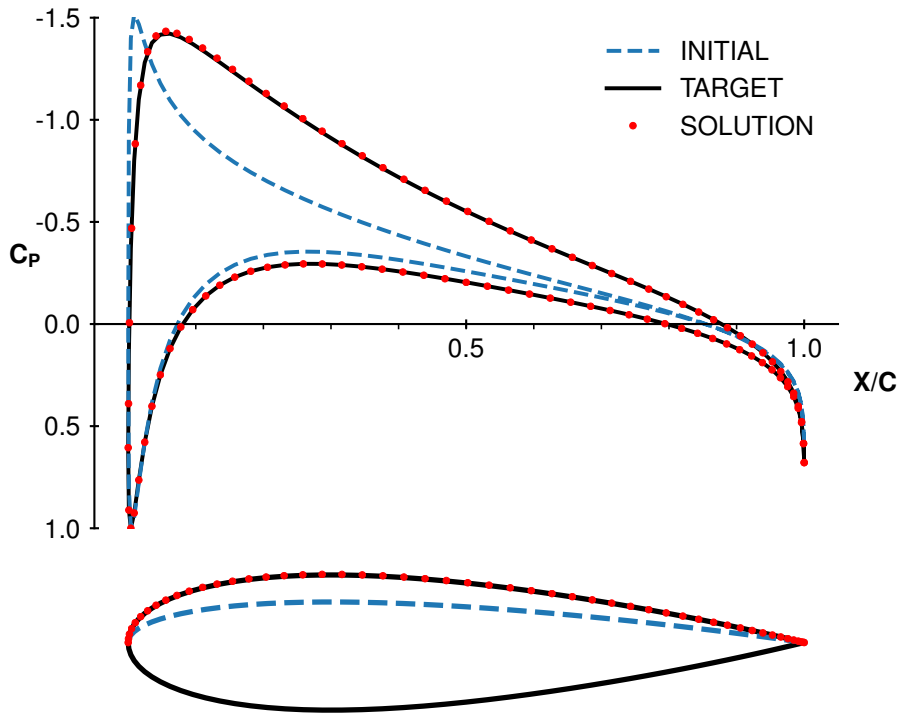


**Fig. 20** Initial, target and solution pressure distributions with their corresponding geometries. Single element design validation case.  $\alpha = 4$ ,  $M = 120$ .

For this case a NACA 0020 airfoil at  $\alpha = 4$ , with  $M = 120$  is used. Figure 20 shows the initial, target and solution pressure distributions with their corresponding geometries. The black line is the regular NACA 0020 pressure distribution, and the dashed blue line the pressure distribution corresponding to the distorted geometry. The specified design

segment correspond to the the dashed blue line, which is the part of the distorted geometry that differs from the regular NACA 0020. In red is the geometry and pressure distribution obtained from the converged solution of the design problem, where the pressure distribution in black was prescribed to the geometry in blue.

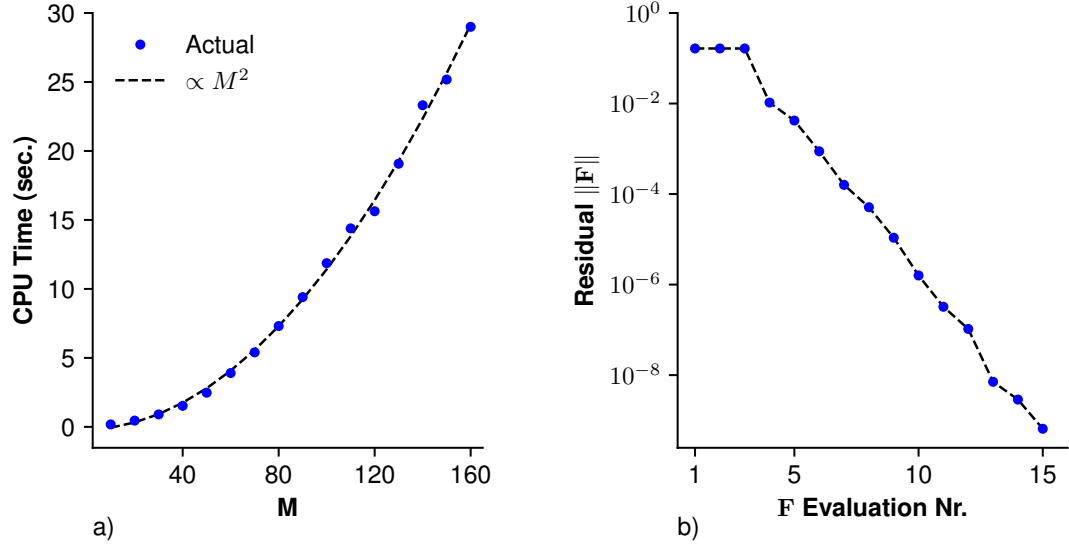


**Fig. 21 (a) Computational requirements as a function of  $M$ . (b) Residual(2-Norm) of the solution progression for  $M = 120$ . Single element design validation case.**

The solution convergence and computational cost for this case is shown in Figure 21. The convergence progression is plotted as the 2-norm of  $F$  at each function evaluation in the Newton-Powell algorithm. A solution path is found almost immediately along which the solution converges steadily. The computational cost is around 60 times higher for a given number of panels compared to a single element analysis case, with approximately 16 seconds needed for a high resolution solution of  $M = 120$ . The detailed computation cost, presented in Table 4 shows the Jacobian evaluation to be the main cost contributor.

$M$	Total CPU Time (sec.)	Nr. of Function Evaluations	Average Time Function Evaluation (sec.)	Nr. of Jacobian Evaluations	Average Time Jacobian Evaluation (sec.)
40	1.5	13	0.03	2	0.54
80	7.3	16	0.14	2	2.36
120	15.6	15	0.30	2	5.27
160	29.0	15	0.55	2	9.82

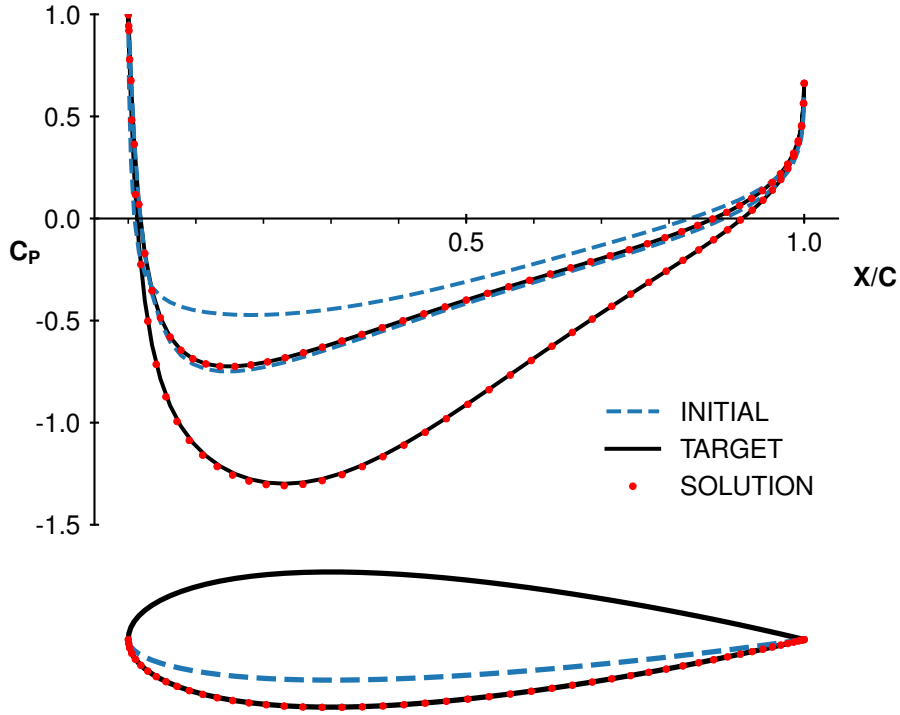
**Table 4 Detailed computational cost for selected  $M$ . Single element design validation case.**

### 5.2.2 Ground Effect Design Validation

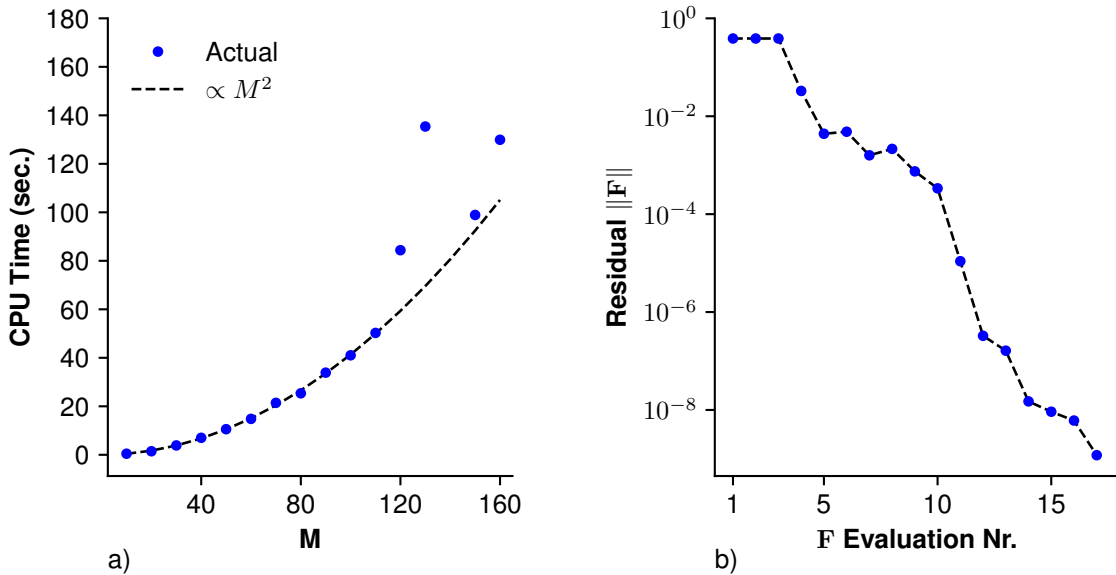
The following cases follow an identical validation process to the single element design validation case and will therefore be covered more briefly.



Figure 22 shows a NACA 0020 airfoil in ground effect at  $h/c = 0.2$ ,  $\alpha = 0$ , with  $M = 120$ . Similar to the previous case, the bottom surface has now been distorted, and the shape is recovered by setting the target pressure distribution to be that of a full NACA 0020 in ground effect. The solution converges to recover the shape of a standard NACA 0020, as expected.



**Fig. 22 Initial, target and solution pressure distributions with their corresponding geometries. Ground effect design validation case.  $h/c = 0.2$ ,  $\alpha = 0$ ,  $M = 120$ .**



**Fig. 23 (a) Computational requirements as a function of  $M$ . (b) Residual(2-Norm) of the solution progression for  $M = 120$ . Ground effect design validation case.**

In this case convergence of the solution becomes more difficult for  $120 \leq M \leq 150$ , where Figure 23 shows a deviation from the trend in the required CPU time for these  $M$ . This

results from the stagnation point being close to the end of the design segment, normally special formulations are required for inverse methods handle cases where the stagnation point is within 2 – 3 boundary points of the design segment end [32]. For the more highly loaded profiles in section 6 this issue is not seen, as the stagnation point is located further along the top surface. The residual shows solution progression to stagnate somewhat after 10 function evaluations, leading to an additional Jacobian evaluation being needed for the solution to converge, as seen in Table 5. For  $M > 150$  the solution goes back to needing only 2 Jacobian evaluations. The large cost of evaluating the Jacobian means that only a single additional evaluation will have a large impact on overall CPU time.

M	Total CPU Time (sec.)	Nr. of Function Evaluations	Average Time Function Evaluation (sec.)	Nr. of Jacobian Evaluations	Average Time Jacobian Evaluation (sec.)
40	7.0	12	0.16	2	2.39
80	25.4	13	0.52	2	8.77
120	84.4	17	1.13	3	20.93
160	129.9	16	2.11	2	45.94

**Table 5 Detailed computational cost for selected  $M$ . Ground effect design validation case.**

### 5.2.3 Multi-Element Design Validation

For validation the design method for multi-element cases the same approach is again used, now considering a tandem arrangement of two distorted NACA 0020 airfoils, as shown in Fig. 24. Ground effect is retained in this validation at  $h/c = 0.2$ ,  $\alpha = 0$ , with  $M = 120$ . The full NACA 0020 shapes are recovered by setting the target pressure distribution for both distorted elements to be that of full NACA 0020s arranged in the same configuration.

A similar increase in the CPU time is seen here as for the previous case, now for  $M \geq 130$  as seen in Fig. 25. Again this is due to the solution becoming more difficult to find for these particular values of  $M$ , and additional Jacobian evaluations are needed to converge the solution, as seen in Table 6.

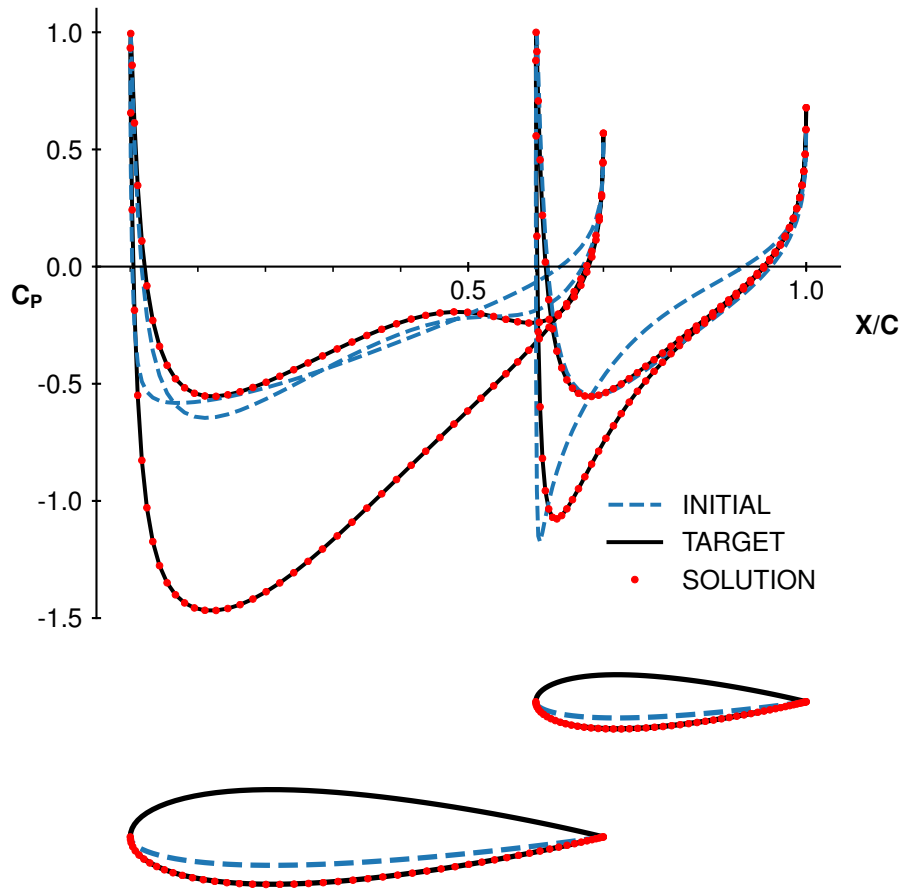


**Fig. 24** Initial, target and solution pressure distributions with their corresponding geometries. Multi-element design validation case.  $h/c = 0.2$ ,  $\alpha = 0$ ,  $M = 120$ .

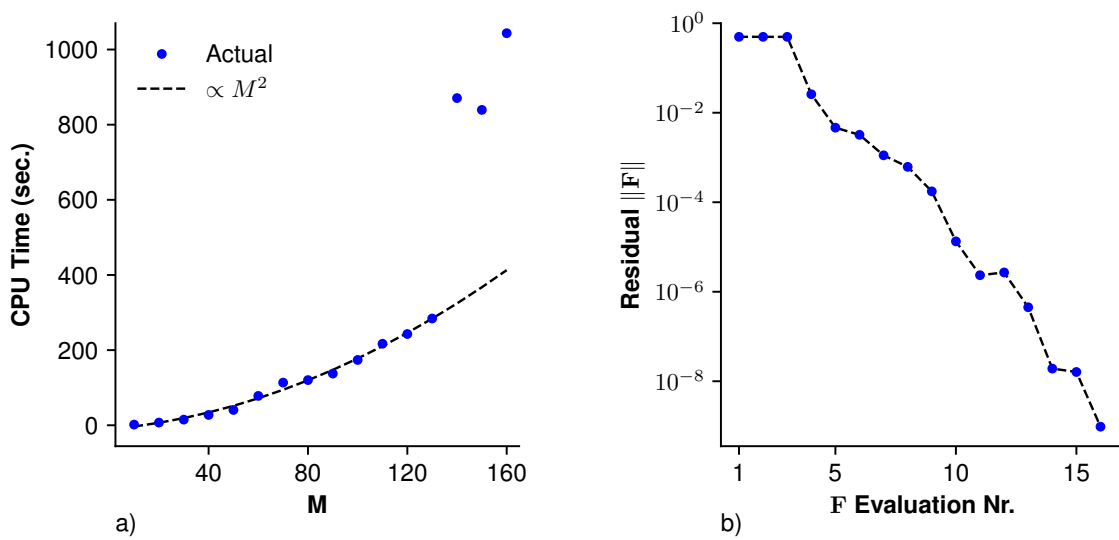


**Fig. 25** (a) Computational requirements as a function of  $M$ . (b) Residual (2-Norm) of the solution progression for  $M = 120$ . Multi-element design validation case.

M	Total CPU Time (sec.)	Nr. of Function Evaluations	Average Time Function Evaluation (sec.)	Nr. of Jacobian Evaluations	Average Time Jacobian Evaluation (sec.)
40	27.5	13	0.59	2	9.21
80	120.3	14	2.17	2	42.30
120	242.9	16	4.36	2	81.83
160	1045.5	25	8.42	5	161.86

**Table 6 Detailed computational cost for selected  $M$ . Multi-element design validation case.**

## 6 Example Design Cases

In this section some typical design cases where the tool can be used are presented. They are meant to display possible design applications where the tool can be used.

### 6.1 Smoothing Surface Pressure Peaks

In section 2.1 the first element was shown to be the most critical in terms of the separation risk, since it is the closest to the ground and therefore most effected by varying ground clearance. In this case any surface pressure peaks at the LE are prone to "runaway" with reduced ground clearance, since the first element does not have a leading element to protect it from this effect. The first element in a section therefore need much attention to avoid these peaks developing.

Two geometries displaying these issues where found in [33], and [14] respectively. The first is originally a super-critical aircraft section designated NLR 7301, that has been inverted here, while the latter has been used on the 1998 Tyrrell 026 F1 car.

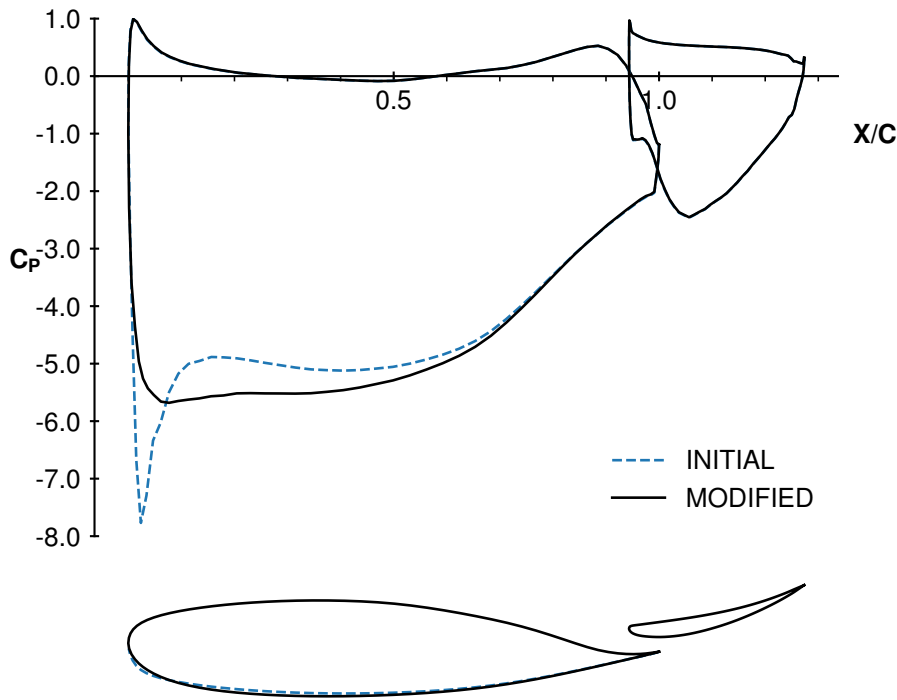


**Fig. 26 Smoothing surface pressure peaks design case. Inverted NRL 7301 wing section.**  $h/c = 0.2$ .

The results for the NLR 7301 wing section is shown in Fig 26, and shows the initial LE peak removed and the pressure distribution smooth. In this case the entire bottom surface of the first element is allowed to move, this is usually necessary when looking for large local changes like this, the entire shape needs to change slightly to achieve a closed profile with the specified local characteristics. This is further demonstrated using this geometry in section 6.3.

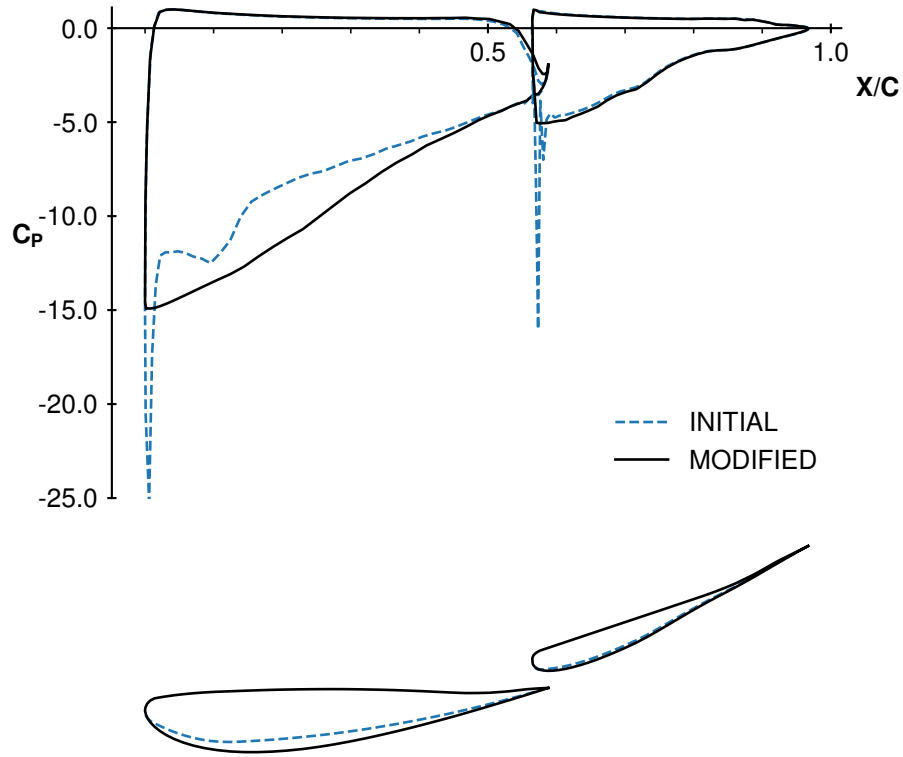


**Fig. 27 Smoothing surface pressure peaks design case. Tyrrell 026 wing section.**  
 $h/c = 0.2$ .

The results for the Tyrrell 026 section is shown in Fig. 27, here both elements are treated in a similar manner simultaneously, as the overlap in this section is too small for the second element to benefit from the circulation of the first. An interactive geometric alteration capability would be useful here to increase the overlap directly within the tool.

## 6.2 Ground Clearance Envelope Optimisation

The critical dependence on ground clearance of a wing section and the adverse pressure gradient on the first element in a section was discussed in section 2.1. Usually there will be a limit to the lowest ground clearance usable before inducing separation on the first element. The inverse design tool can be used to optimise this behaviour, by specifying a pressure distribution with relatively benign gradients at the lowest ground clearance in the intended operation envelope, here taken as  $h/c = 0.105$ . This is shown using the Tyrrell 026 wing section in Fig. 28.

The pressure distributions of the original and modified sections are shown for high and low ground clearances in Fig. 29, Fig. 30, and Fig. 31, Fig. 32, respectively. Here the ground clearances from [14] are used. For the modified section  $h/c \leq 0.105$  now has a desirable trend. Going lower than this to  $h/c = 0.079$ , the pressure distribution again starts to display issues. For optimal use in this a viscous model would be required for predicting separation in these types of cases. The gradient could then be tuned to be used to its maximum at the lowest ground clearance.

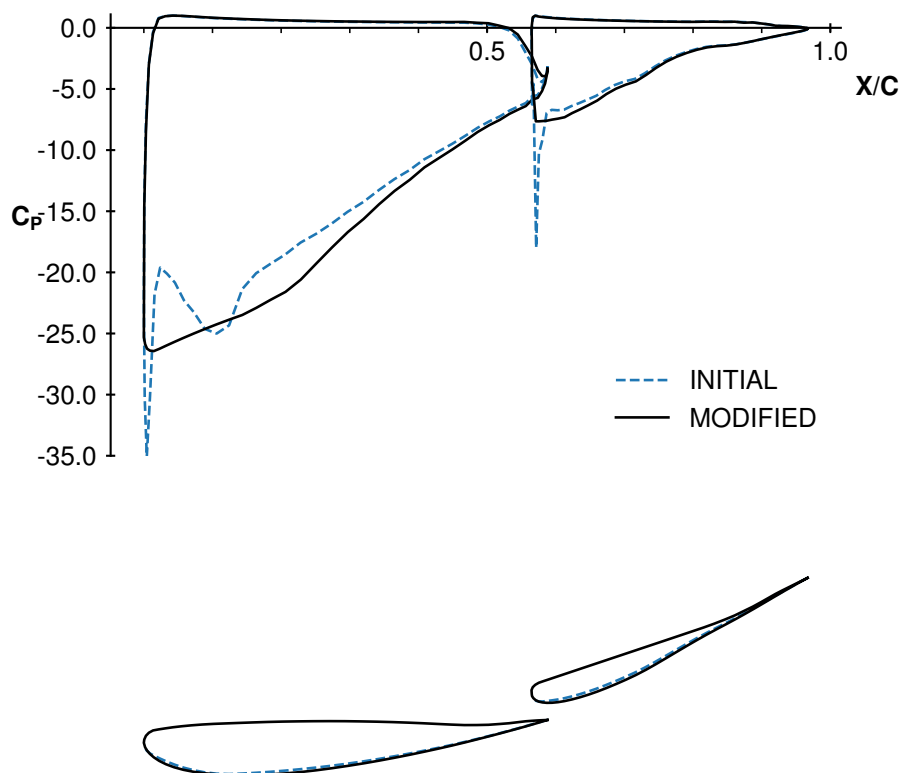


Fig. 28 Specified pressure distribution at the lowest ground clearance in the intended operational envelope,  $h/c = 0.105$ .

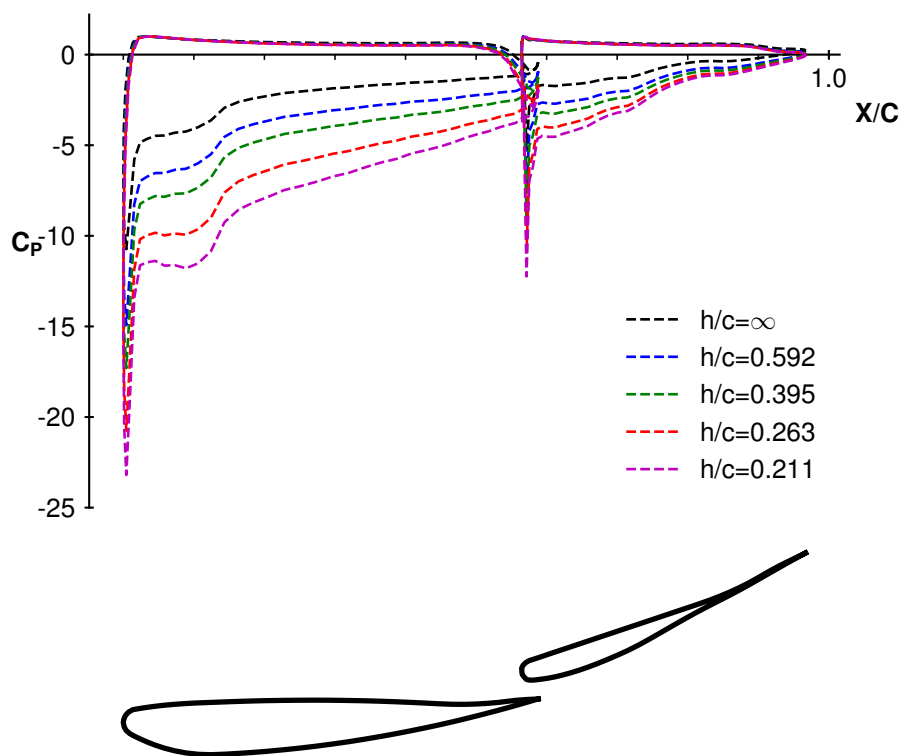
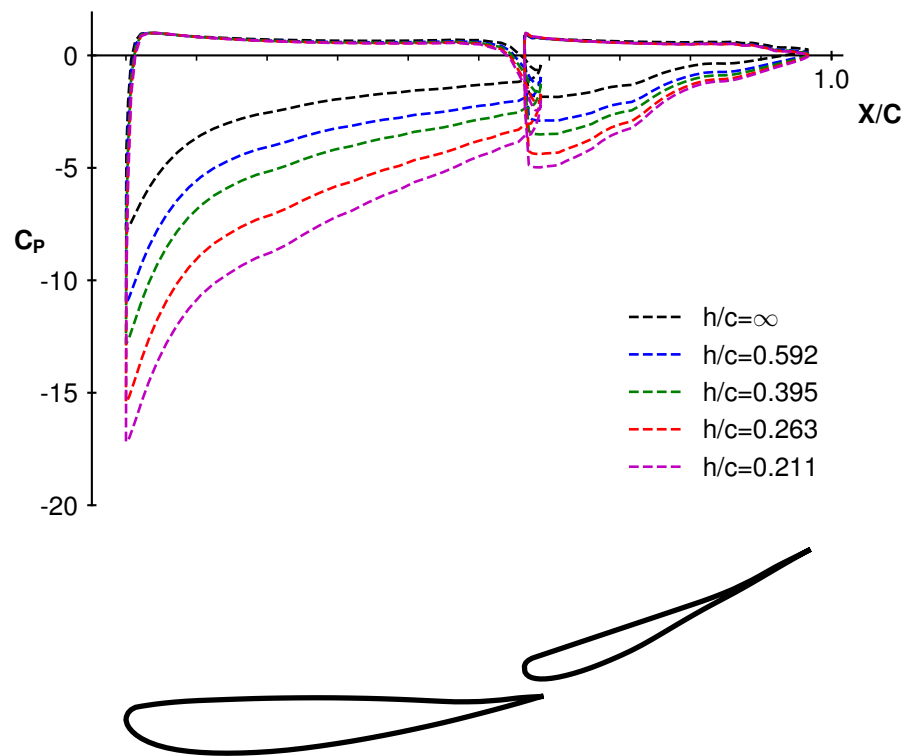
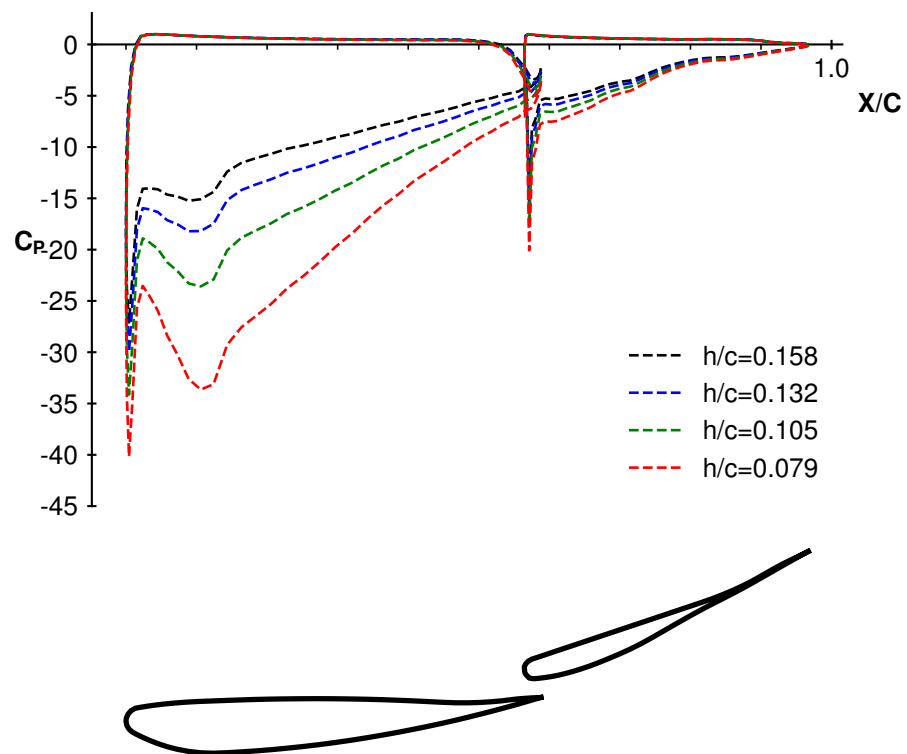


Fig. 29 Pressure distributions for upper range of ground clearances. Initial Tyrrell 026 wing section.



**Fig. 30 Pressure distributions for upper range of ground clearances. Modified Tyrrell 026 wing section.**



**Fig. 31 Pressure distributions for lower range of ground clearances. Initial Tyrrell 026 wing section.**



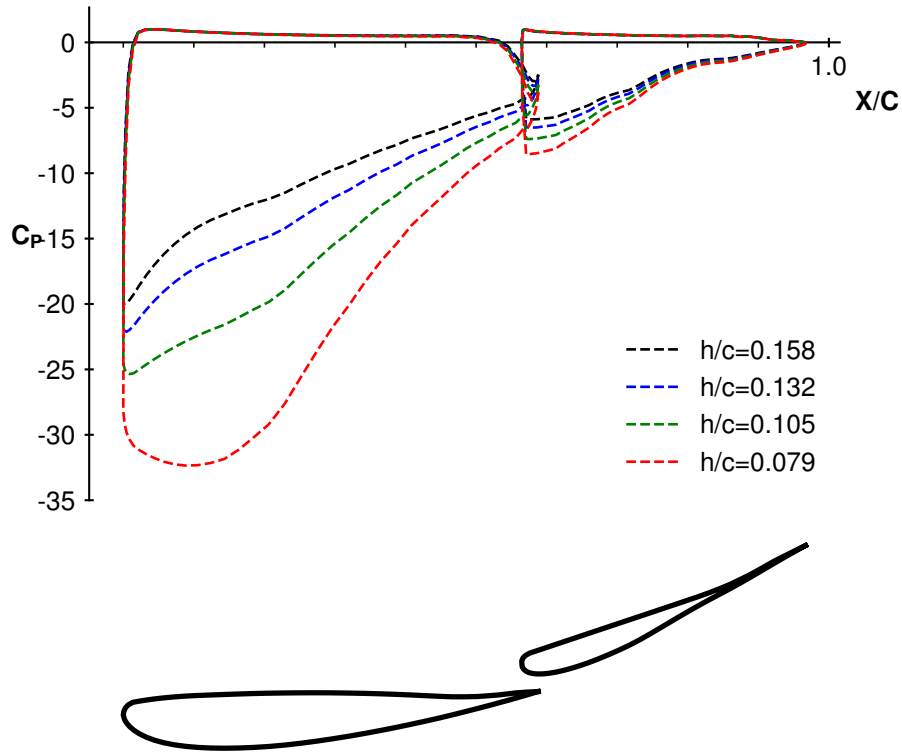


**Fig. 32 Pressure distributions for lower range of ground clearances. Modified Tyrrell 026 wing section.**

### 6.3 Demonstration of Pressure Distribution Degrees of Freedom (A and B constants)

The argument for allowing two degrees of freedom to the specified pressure distribution was presented in section 4.3. Here this demonstrated using the NRL 7301 design case from section 6.1. The intuitive approach to removing the pressure peak in this case is to specify a distribution that simply "cuts" it away as indicated in red in Fig. 33. However, this distribution is not compatible with the fixed part of the geometry at the LE, and if no freedom is allowed,  $A = B = 0$ , the resulting geometry has a non-smooth profile.

Cases where allowing freedom in the pressure distribution are shown in Fig. 34, and Fig. 35. In the former, only the design segment is specified to span over the region close to the LE only. This results in a solution where the peak is smoothed, but not eliminated. To achieve this, a larger portion of the geometry needs to be allowed to change as in the latter case. Here a pressure distribution with no peak is obtained. This distribution is different to what was specified, but is the solution that is both compatible with the fixed part of the geometry and eliminates the pressure peak.

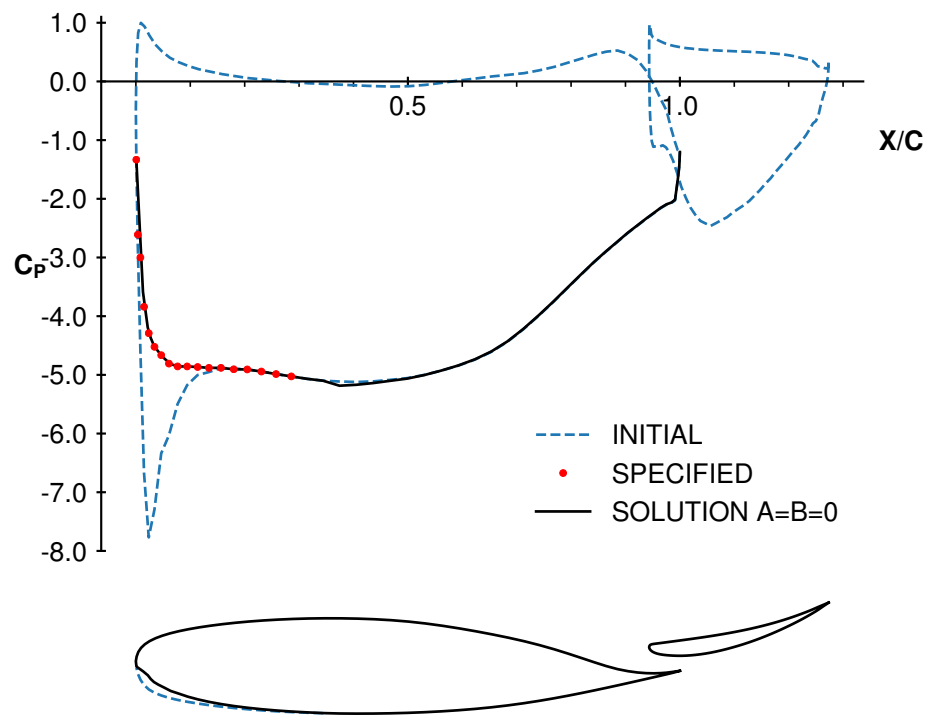


**Fig. 33** Forcing the exact specified pressure distribution by setting  $A = B = 0$ .

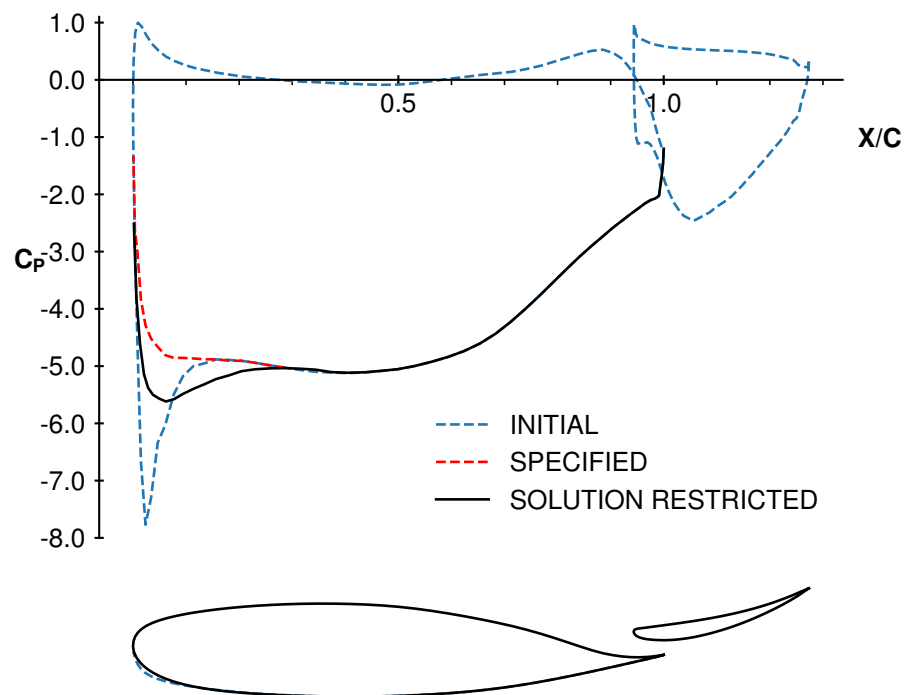


**Fig. 34** Allowing movement over a short section of the surface only.

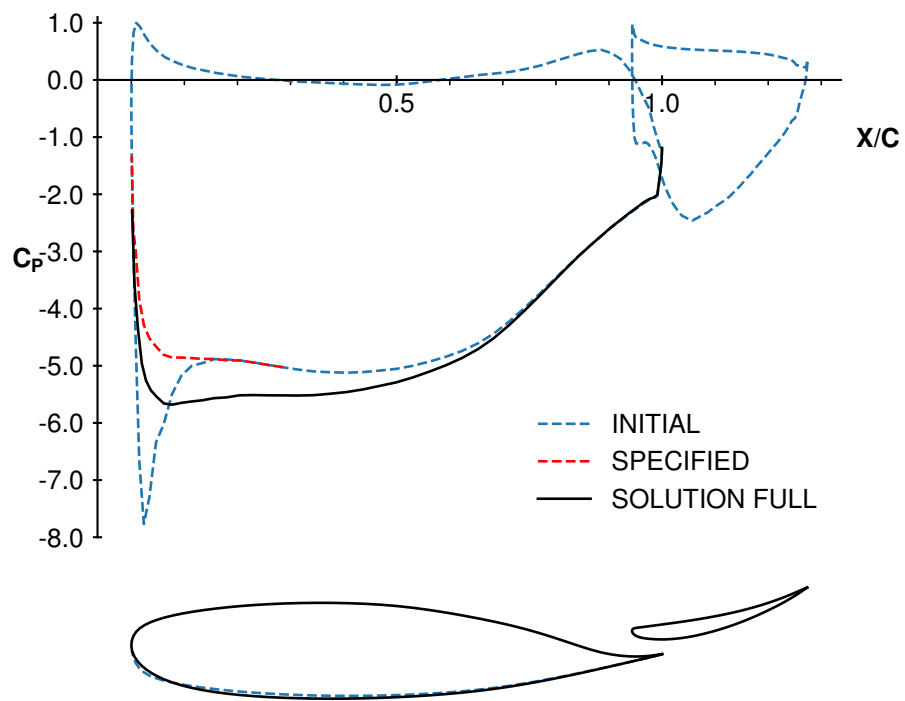


**Fig. 35** Allowing movement over the entire surface.

#### 6.4 Representative Analysis and Design Case: Scuderia Toro Rosso STR10 Y-400 Front Wing Section

In this section the capability of the tool to perform analysis on and solve design problems for a representative Formula 1 multi-element wing section will be briefly shown. This wing section was supplied by the Scuderia Toro Rosso Aerodynamics Department and originates from their 2015 car STR10, where it was used as the sectional profile of the front wing at 400mm span.

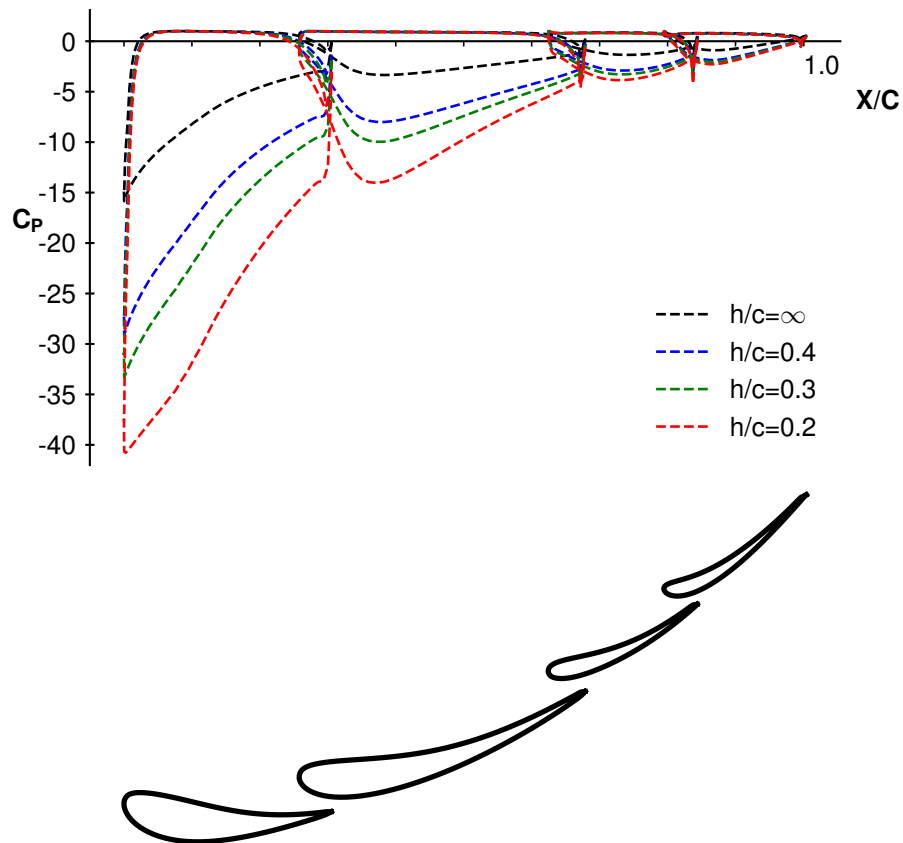


**Fig. 36 Analysis example for STR10 Y-400 front wing section. Pressure distribution for varying ground clearances shown.**

Figure 36 shown an analysis example using the geometry. The benefits of the circulation from elements mounted in front of other can be seen well. The pressure distributions of trailing elements takes a laminar airfoil like shape, which is beneficial for gradients when  $h/c$  reduces. Large overlaps of elements are used to make best use of this effect. Using  $M=120$ , this case requires 17-seconds of CPU time per ground clearance.

The  $C_Z$  variation with ground clearance for each element and the total section is shown in Fig. 37. These values are normalised with their free-flow values i.e. the values out of ground effect. The forward elements are most effected.

A design example is shown in Fig. 38. This section displays no obvious issues, and the design modification made is only for illustrative purposes. In this case the bottom surfaces of the first two elements are modified. This requires 11-minutes of CPU time to converge using  $M = 120$ .

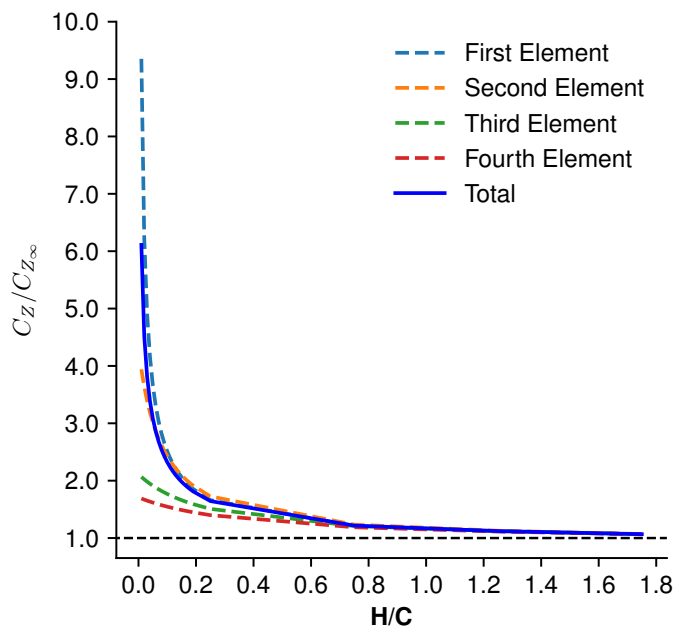


**Fig. 37** Variation in  $C_Z$  for varying ground clearances. STR10 Y-400 front wing section. The individual elements  $C_Z$  in normalised using its free-flow value.

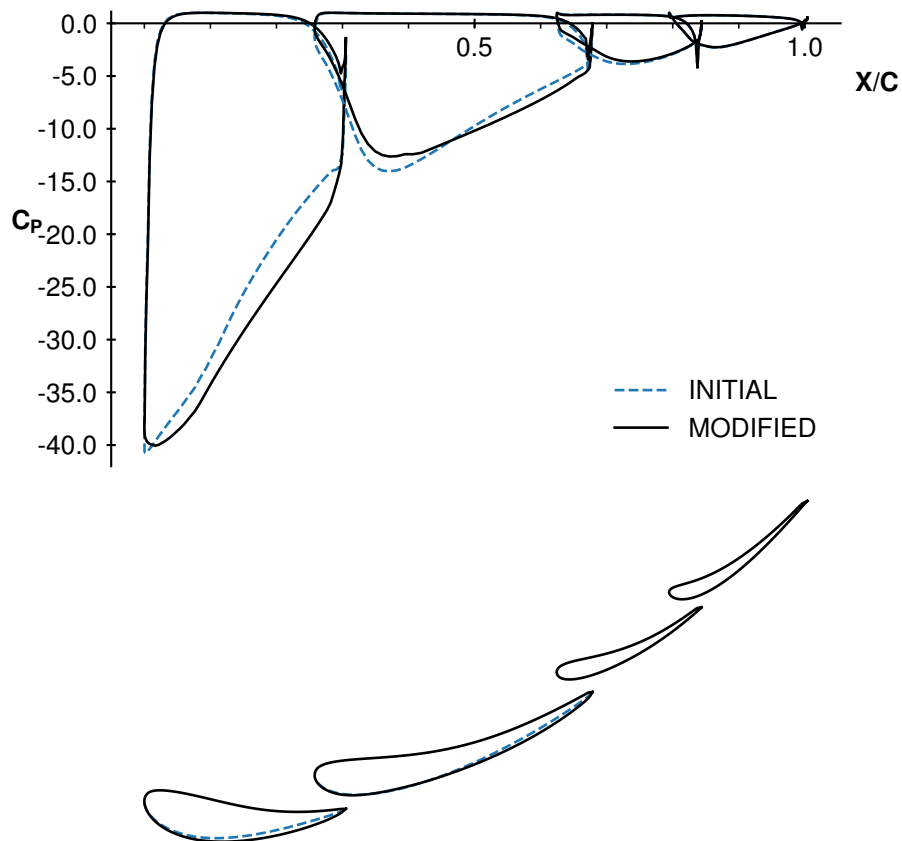


**Fig. 38** Design example for STR10 Y-400 front wing section. Initial and modified pressure distributions shown.

## 6.5 Post-Processing Examples

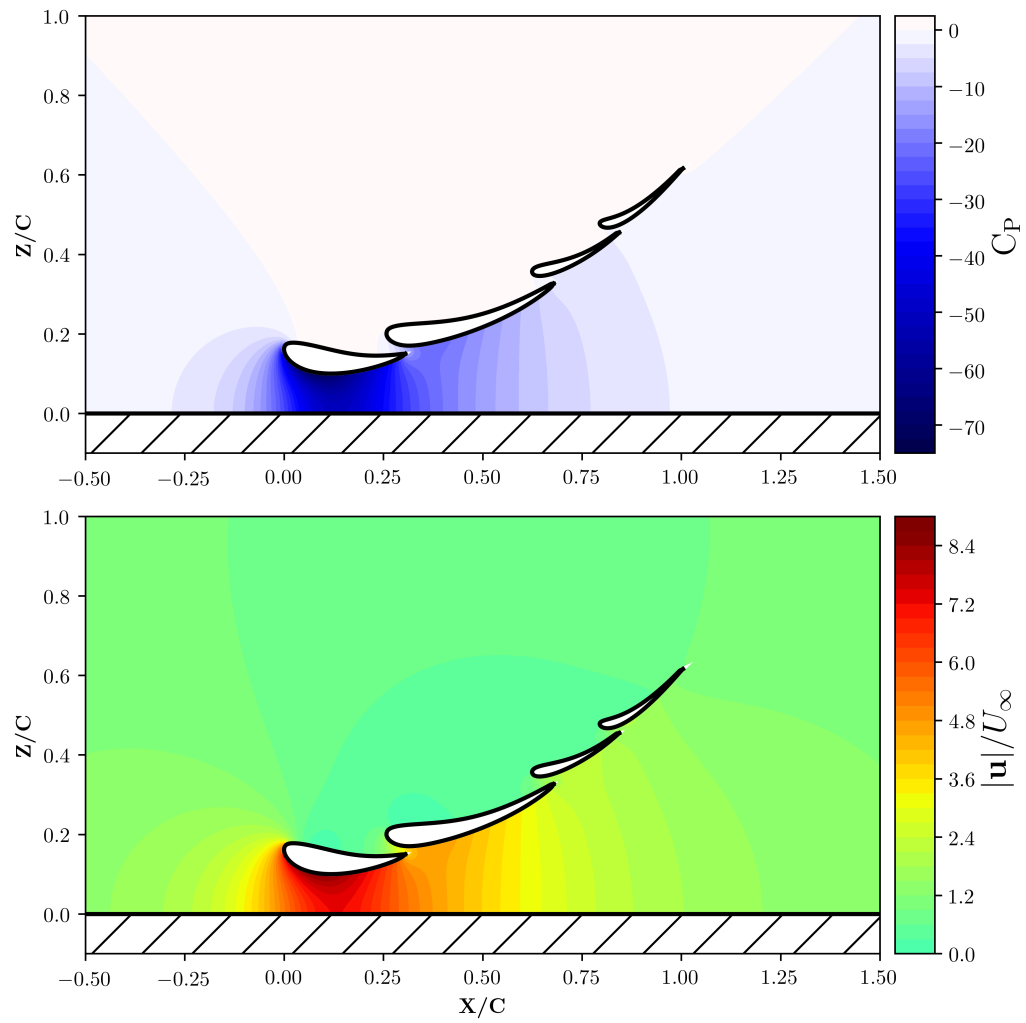


**Fig. 39**  $C_P$  and velocity fields. STR10 Y-400 front wing section.  $h/c = 0.1$ .

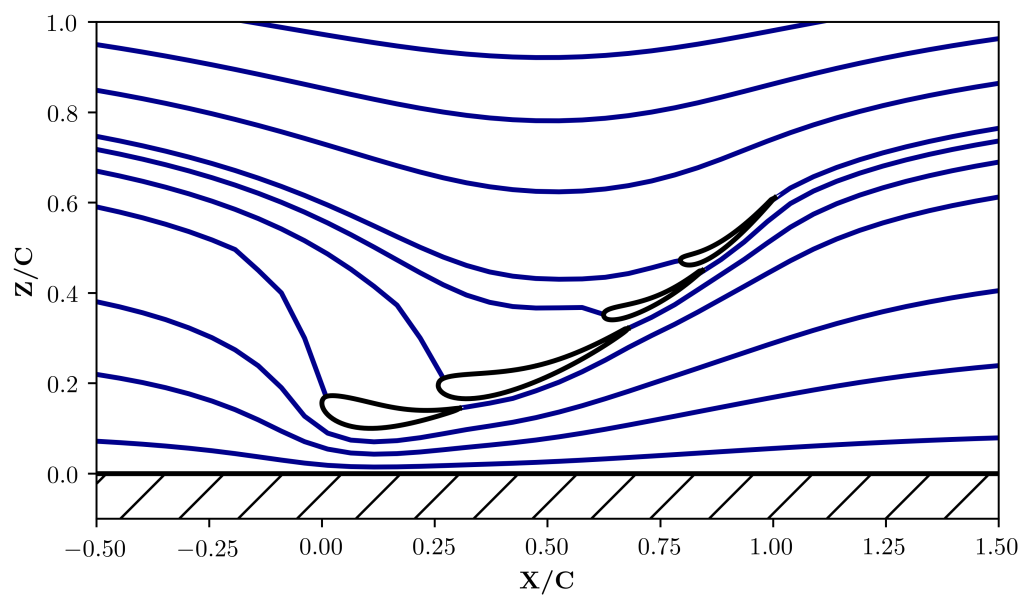


**Fig. 40** Streamlines. STR10 Y-400 front wing section.  $h/c = 0.1$ .

## 7 Discussion on Limitations

In this section the main limitations of the tools implementation is considered based on the various cases presented in sections 5 and 6. Some possible methods for over coming them are discussed.

Two of the cases in section 5 saw convergence issues for some  $M$  due to the stagnation point being too close to, or on the edge of the design segment. This is a common problem in inverse methods [32]. In the formulation of Eq. (52),  $\gamma_i$  is the sum of two quadratics functions with one degree of freedom each.  $\gamma_i$  can thus be guaranteed to take two specific values over the design segment by setting the values of  $A$  and  $B$ . This is normally used to match the required  $\gamma_i$  values at the ends of the segment to ensure smoothness of the profile. If a stagnation point occurs on, or very close to the design segment, it forces  $\gamma_i$  to take a zero ( $C_p = 1$ ) or very close to zero value at this point, which can be considered "using up" one of the available degrees of freedom. A solution for the  $\gamma$ -distribution compatible with the fixed part of the geometry can not be guaranteed.

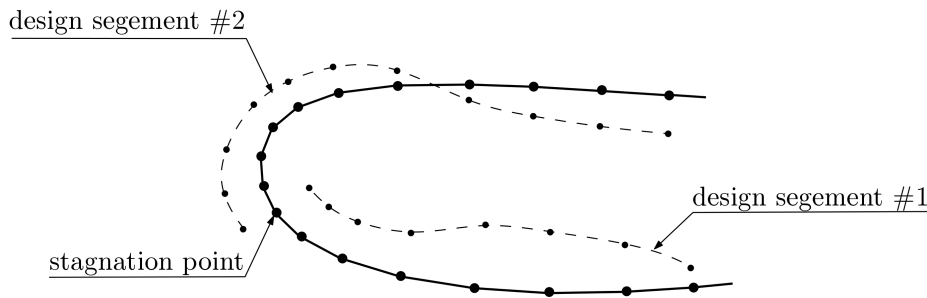


**Fig. 41 Floated stagnation point**

To remove this sensitivity the stagnation point can be floated in the solution, as the end point of one design segment, and the start point of another, as shown in Fig. 41. To achieve a closed system using two design segments both segments can be extended to also coincide at the TE. This leads to an inverse model where the pressure distribution is prescribed over the entire element with the TE position fixed. This way there is no need to introduce a unique set of constants  $A$  and  $B$  constants for the second design as continuity is achieved by both segments for the same  $A$  and  $B$  if they form a closed loop. This system would thus be closed using the current formulation of this work.

If it is desired to have some part of the geometry fixed, two unique degrees of freedom are required for the second design segment, and two additional relations need to be found for closing the system. This can be done by fixing the position of two additional boundary points inside the inverse segments, requiring no movement of these points in the solution. For example, applying Eqs.(48,49) at both  $i = i_S$ , and  $i = i_S + 1$  for the first segment and, at both  $i = i_E$  and  $i = i_E - 1$  for the second, similar to what is described in [32].

The biggest limitations naturally lie in the prediction of physics that are not accounted for in the model. A very simple model was chosen to ensure the computational cost to be very low, and thus only potential 2D-flow is considered. There are however very cost efficient ways of predicting viscous boundary layer effects in combination with panel-methods that would not increase the computational time substantially [8]. These methods are based on a

simplified Navier-Stokes Equation valid for thin boundary-layers, where the viscous solution is computed near the surface of the geometry and coupled with the potential-flow model at the edge of the boundary-layer by a so called viscous-inviscid interaction model.

Such an implementation could be used to great effect for design cases like in Section 6.2. The inverse method could be re-formulated solve a geometry of specified skin friction distributions, effectively optimising the pressure gradient to extract the maximum possible  $C_z$  of a profile before separation is induced.

In the same design case it was noted that the overlap of the trailing element was not large enough to benefit from the leading elements circulation to reduce pressure peaks at the LE. For such cases, an interface for modification of the geometry would be beneficial. The overlap could be set manually by translating the trailing element and then the interaction optimised using the inverse design tool.



## 8 Summary, Conclusions and Outlook

An inverse design tool for multi-element wing section in ground effect has been developed and validated. Its formulation is based on potential-flow theory and was developed around the design considerations of Formula 1 front wings in particular, but is applicable to any wing section. This tool is proposed to compliment traditional CFD methods in solving typical design problems, where solutions can be specified as a pressure distribution. Some example cases solving such problems have been shown. The tool is implemented as a Python computer program and made available through GitHub [here].

Based on the work presented in this report it is concluded that:

- 1) The analysis method of the tool developed is capable of predicting the aerodynamics of multi-element wing-sections in accordance to potential-flow theory.
- 2) The design method of the tool developed is capable of finding the geometry of a wing section corresponding a pressure distribution prescribed over a single section of each element, providing this section does not contain a stagnation point. The geometry obtained from solving the design method corresponds to the continuous and smooth body with a pressure distribution closest to the prescribed pressure distribution.
- 3) The computational cost solving relevant design cases is low enough for the tool to be used interactively in the design process. Especially a more powerful workplace desktop machine, where computational times would be significantly lower than what is presented in this report.

Based on the limitations found through the usage of the tool in section 5 and section 6, and later discussed in section 7, for further development of this tool the following is recommended:

- 1) Implementation of the method described in section 7 for handling stagnation points inside design segments. This would increase the robustness of the tool while extending its capabilities to prescribing pressure distributions over entire elements.
- 2) An interface for interactive modification of the sectional geometry inside the tool. Designs could then be rapidly iterated by a mix of manual modifications and inverse design.
- 3) An extension of the tool to consider viscous effects in the boundary layer using a viscous-inviscid interaction model.

## References

- [1] FIA, "FORMULA ONE-TECHNICAL REGULATIONS-2019." <https://www.fia.com/regulation/category/110>, 2018. Accessed 9 Dec. 2018.
- [2] FIA, "FORMULA ONE-SPORTING REGULATIONS-2019." <https://www.fia.com/regulation/category/110>, 2018. Accessed 9 Dec. 2018.
- [3] Jameson, A., "Full-Potential, Euler, and Navier-Stokes Schemes." *Applied Computational Aerodynamics. Vol. 125 of Progress in Aeronautics and Astronautics*, Vol. 125, 1990, pp. 39–88.
- [4] Smith, A. M. O., "The Panel Method: Its Original Development." *Applied Computational Aerodynamics. Vol. 125 of Progress in Aeronautics and Astronautics*, Vol. 125, 1990, pp. 3–14.
- [5] Hess, J. L., and Smith, A. M. O., "Calculation of Potential Flow about Arbitrary Bodies." *Vol. 8, Progress in Aeronautics and Astronautics*, Vol. 8, 1966, pp. 1–138.
- [6] Geising, J. P., and Smith, A., "Potential Flow about Two-Dimensional Hydrofoils." *Journal of Fluid Mechanics*, Vol. 28, 1967, pp. 113–129.
- [7] Leibbeck, R., "Subsonic Airfoil Design." *Applied Computational Aerodynamics. Vol. 125 of Progress in Aeronautics and Astronautics*, Vol. 125, 1990, pp. 133–165.
- [8] Drela, M., "XFOIL: An Analysis and Design System for Low Reynolds Number Airfoils." *Low Reynolds Number Aerodynamics: Proceedings of the Conference Notre Dame, Indiana, USA, 5–7 June, 1989*, pp. 1–12.
- [9] Hepperle, M., "JAVAFOIL User's Guide," 2019.
- [10] Smith, A. M. O., "High-Lift Aerodynamics." *Journal of Aircraft*, Vol. 12, No. 6, 1975, pp. 501–530.
- [11] Zerihan, J., and Zhang, X., "Aerodynamics of a Single Element Wing in Ground Effect.." *Journal of Aircraft*, Vol. 37, No. 6, 2000, pp. 1058–1064.
- [12] Zerihan, J., and Zhang, X., "Aerodynamics of a Double-Element Wing in Ground Effect," *AIAA Journal*, Vol. 41, No. 6, 2003, pp. 1007–1016.
- [13] Mahon, S., and Zhang, X., "Computational Analysis of a Inverted Double-Element Airfoil in Ground Effect." *Journal of Fluids Engineering*, Vol. 128, No. 6, 2006, pp. 1172–1180.
- [14] Zerihan, J., "An Investigation into the Aerodynamics of Wings in Ground Effect." Ph.D. thesis, University of Southampton, School of Engineering Sciences, 2001.
- [15] Newbon, J., Dominy, R. G., and Sims-Williams, D., "CFD investigation of the effect of the salient flow features in the wake of a generic open-wheel race car." *SAE International Journal of Passenger Cars- Mechanical Systems*, Vol. 1, 2015, pp. 217–232.
- [16] Katz, J., and Plotkin, A., *Low-speed aerodynamics. 2nd ed.*, Cambridge University Press, Cambridge, 2001.
- [17] Yon, S., Katz, J., and Plotkin, A., "Effect of airfoil (trailing-edge) thickness on the numerical solution of panel methods based on the Dirichlet boundary condition.." *AIAA Journal*, Vol. 30, No. 3, 1992, pp. 697–702.
- [18] Goude, A., and Engblom, S., "A general high order two-dimensional panel method." *Applied Mathematical Modelling*, Vol. 60, 2018, pp. 1–17.

- [19] Morino, L., and Kuo, C., "Subsonic Potential Aerodynamics for Complex Configurations : A General Theory.." *AIAA Journal*, Vol. 12, No. 2, 1974, pp. 191–197.
- [20] Boschetti, P., Quijada, G., and Cárdenas, E., "Dynamic Ground Effect on the Aerodynamic Coefficients Using a Panel Method.." *Journal of Aircraft*, Vol. 54, No. 2, 2017, pp. 838–844.
- [21] Dragos, L., "Numerical solution of the equation for a thin airfoil in ground effect.." *AIAA Journal*, Vol. 28, No. 12, 1990, pp. 2132–2134.
- [22] Rostami, A., Ghadimi, P., and Ghasemi, H., "Adaptive viscous–inviscid interaction method for analysis of airfoils in ground effect.." *Journal of the Brazilian Society of Mechanical Sciences and Engineering*, Vol. 38, No. 6, 2016, pp. 1593–1607.
- [23] Johnson, F., "A General Panel Method for the Analysis and Design of Arbitrary Configurations in Incompressible Flows." *NASA CR 3079*, 1980.
- [24] Labrujere, T., and Slooff, J., "Computational Methods for the Aerodynamic Design of Aircraft Components.." *Annual Review of Fluid Mechanics*, Vol. 25, No. 1, 1993.
- [25] Yiu, K., "Computational methods for aerodynamic shape design." *Mathematical and Computer Modelling*, Vol. 20, No. 12, 1994.
- [26] Henne, P., "An inverse transonic wing design method.." *18th Aerospace Sciences Meeting*, 1980.
- [27] Maskew, B., "Program VSAERO Theory Document.." *NASA CR 4023*, 1987.
- [28] Eppler, R., and Somers, D. M., "A Computer Program for the Design of Low-Speed Airfoils." *NASA TM 80210*, Aug. 1980.
- [29] Volpe, G., and Melnik, R. E., "The Design of Transonic Airfoils by a Well-Posed Inverse Method." *International Conference on Inverse Design Concepts in Engineering Sciences*, 1984.
- [30] Moré, J. J., Garbow, B. S., and Hillstom, K. E., "User Guide for MINPACK-1." *ANL-80-74*, 1980, pp. 17–21.
- [31] Suddhoo, A., and Hall, I. M., "Test Cases for the Plane Potential Flow Past Multi-Element Airfoils." *Aeronautical Journal*, Vol. 89, No. 890, Dec. 1985, pp. 403–414.
- [32] Drela, M., "Two-dimensional transonic aerodynamic design and analysis using the Euler equations." Ph.D. thesis, Massachusetts Institute of Technology, Dept. of Aeronautics and Astronautics, 1986.
- [33] Weber, S., and Platzer, M., "Computational simulation of dynamic stall on the NLR 7301 airfoil," *Journal of Fluids and Structures*, Vol. 14, 2000, pp. 779–798. doi:10.1006/jfls.2000.0299.